

1   **Title** The orchestrated cellular and molecular responses of the kidney to endotoxin define the  
2   sepsis timeline

3   **Authors:** Danielle Janosevic,<sup>1</sup> Jered Myslinski,<sup>1</sup> Thomas McCarthy,<sup>1</sup> Amy Zollman,<sup>1</sup> Farooq  
4   Syed,<sup>2</sup> Xiaoling Xuei,<sup>3</sup> Hongyu Gao,<sup>3</sup> Yunlong Liu,<sup>3</sup> Kimberly S. Collins,<sup>1</sup> Ying-Hua Cheng,<sup>1</sup> Seth  
5   Winfree,<sup>1</sup> Tarek M. El-Achkar,<sup>1,4</sup> Bernhard Maier,<sup>1</sup> Ricardo Melo Ferreira,<sup>1</sup> Michael T. Eadon,<sup>1</sup>  
6   Takashi Hato,<sup>1, 5, \*</sup> Pierre C. Dagher<sup>1,4, \*</sup>

7   <sup>1</sup>Department of Medicine, Indiana University School of Medicine

8   <sup>2</sup>Department of Pediatrics and the Herman B Wells Center, Indiana University School of  
9   Medicine

10   <sup>3</sup>Department of Medical and Molecular Genetics, Indiana University School of Medicine

11   <sup>4</sup>Roudebush Indianapolis Veterans Affairs Medical Center, Indianapolis, Indiana, USA.

12   <sup>5</sup>Lead Contact

13   \*Correspondence: [thato@iu.edu](mailto:thato@iu.edu) (TH), [pdaghe2@iu.edu](mailto:pdaghe2@iu.edu) (PCD)

14

## 15   **Abstract**

16   Clinical sepsis is a highly dynamic state that progresses at variable rates and has life-  
17   threatening consequences. Staging patients along the sepsis timeline requires a thorough  
18   knowledge of the evolution of cellular and molecular events at the tissue level. Here, we  
19   investigated the kidney, an organ central to the pathophysiology of sepsis. Single cell RNA  
20   sequencing revealed the involvement of various cell populations in injury and repair to be  
21   temporally organized and highly orchestrated. We identified key changes in gene expression  
22   that altered cellular functions and can explain features of clinical sepsis. These changes  
23   converged towards a remarkable global cell-cell communication failure and organ shutdown at a  
24   well-defined point in the sepsis timeline. Importantly, this time point was also a transition  
25   towards the emergence of recovery pathways. This rigorous spatial and temporal definition of  
26   murine sepsis will uncover precise biomarkers and targets that can help stage and treat human  
27   sepsis.

28

29 **Introduction**

30 Acute kidney injury (AKI) is a common complication of sepsis that doubles the mortality risk. In  
31 addition to failed homeostasis, kidney injury can contribute to multi-organ dysfunction through  
32 distant effects. Indeed, the injured kidney is a significant mediator of inflammatory chemokines,  
33 cytokines, and reactive oxygen species that can have both local as well as remote deleterious  
34 effects<sup>1-4</sup>. Therefore, understanding the complex pathophysiology of kidney injury is crucial for  
35 the comprehensive treatment of sepsis and its complications.

36 We have recently shown that renal injury in sepsis progresses through multiple phases. These  
37 include an early inflammatory burst followed by a broad antiviral response and culminating in  
38 translation shutdown and organ failure<sup>5</sup>. In a non-lethal and reversible model of endotoxemia,  
39 organ failure was followed by spontaneous recovery. The exact cellular and molecular  
40 contributors to this multifaceted response remain unknown. Indeed, the kidney is architecturally  
41 a highly complex organ in which epithelial, endothelial, immune and stromal cells are at  
42 constant interplay. Therefore, we now examined the spatial and temporal progression of  
43 endotoxin injury to the kidney using single cell RNA sequencing (scRNASeq). Our data revealed  
44 that cell-cell communication failure is a major contributor to organ dysfunction in sepsis.  
45 Remarkably, this phase of communication failure was also a transition point where recovery  
46 pathways were activated. We believe this spatially and temporally anchored approach to sepsis  
47 pathophysiology is crucial for identifying potential biomarkers and therapeutic targets.

48

49

50

51

52 **Results**

53 *Single cell RNA sequencing and spatial transcriptomics identify and localize known and novel*  
54 *renal cell populations*

55 We harvested a cumulative amount of 63,287 renal cells obtained at 0, 1, 4, 16, 27, 36 and 48  
56 hours after endotoxin (LPS) administration. The majority of renal epithelial, immune and  
57 endothelial cell types were represented (**Fig. 1a**). Note the absence of podocyte and mesangial  
58 cells, which can be a limitation of single cell RNAseq renal dissociation procedures<sup>6</sup>. Cluster  
59 identities were assigned and grouped using known classical phenotypic markers (**Fig. 1b**,  
60 **Supplementary Fig. 1a**)<sup>7-11</sup>. Interestingly, the UMAP-based computational layout of epithelial  
61 clusters recapitulated the normal tubular segmental order in the nephron. This indicates that  
62 gene expression gradually changes among neighboring tubular segments along the nephron.  
63 Note that the expression of cluster-defining markers varied significantly during the injury and  
64 recovery phases of sepsis (**Fig. S1b; Supplementary Table 1**). Therefore, we also identified a  
65 set of genes that are conserved across time for a given cell type (**Fig. S1c**).

66 In the integrated UMAP (**Fig. 1a**), we noted the presence of a proliferative cell cluster (*Cdk1* and  
67 *Ki67* expression). By back mapping to time-specific unintegrated UMAPs, we determined that  
68 these proliferating cells could be traced to specific cell types at various points along the sepsis  
69 timeline (**Fig. 1c**). For example, within the first hour after LPS, these proliferative indices were  
70 expressed primarily in S1 cells. These cells are the site of LPS uptake in the kidney as we have  
71 previously shown<sup>12-14</sup>. At later time points, proliferative indices are seen in macrophages (4  
72 hours) and S3 cells (36 hours) (**Fig. 1c**). These proliferative indices reflect cell cycle activity  
73 which may be involved in injury, repair or recovery processes<sup>15</sup>.

74 We also noted the presence of a proximal tubular cluster expressing unique gene identifiers:  
75 *Agt*, *Rnf24*, *Slc22a7* and *Slc22a13* (**Fig. 2a**). This is likely the proximal tubular S3-Type 2

76 (S3T2) reported by others<sup>16</sup>. This cluster maintained a separate and distinct identity throughout  
77 the sepsis timeline (**Fig. 1c**). Because the location of S3T2 is currently unknown, we performed  
78 in-situ spatial transcriptomics on septic mouse kidneys<sup>17</sup>. We then integrated our scRNAseq  
79 with the in-situ RNAseq in order to map our scRNAseq clusters onto the tissue (**Supplementary**  
80 **Fig. 2a, S2b**). We found that the classical S3 cluster localizes to the cortex while S3T2 is in the  
81 outer stripe of the outer medulla (**Fig. 2b, Supplementary Fig. 2b**). We confirmed the location  
82 of S3T2 to the OS-OM with single molecular FISH (**Supplementary Fig. 2c**). The differential  
83 gene expression between S3 and S3T2 is likely dictated by regional differences in the  
84 microenvironments of the cortex and the outer stripe.

85 Because angiotensinogen (*Agt*) was strongly expressed in S3T2, we examined the expression  
86 of other components of the renin-angiotensin system (RAS). We first noted the absence of Ace  
87 expression in S1 tubular cells (**Fig. 2c, Supplementary Fig. 3**). In contrast, Ace2 was strongly  
88 expressed in S1, S3 and S3T2 cells. There is currently great interest in understanding the  
89 biology of Ace2 because of its role in SARS-CoV-2 cellular invasion. Other essential  
90 components of the SARS-CoV-2 entry mechanism include *Tmprss2* and *Slc6a19*<sup>18-22</sup>. While  
91 *Tmprss2* was expressed in all proximal tubular segments, *Slc6a19* was more strongly  
92 expressed in S1 throughout the sepsis timeline. This may point to the S1 tubular segment as  
93 one point of entry of SARS-CoV-2 into the kidney.

94 *Cell trajectory and velocity field analyses of scRNAseq characterize subpopulations of immune*  
95 *cells*

96 The immune cell profile in the septic kidney was time-dependent and showed a five-fold  
97 increase in immune cells, primarily macrophages (**Fig. 3a, 3b**). We noted two distinct  
98 macrophage clusters denoted as Macrophage A and Macrophage B (Mφ-A, Mφ-B). Both of  
99 these clusters expressed classical macrophage markers such as Cd11b (*Itgam*) (**Fig. 3c**).  
100 However, they differed in the expression of *Adgre1* (F4/80, Mφ-A) and *Ccr2* (Mφ-B). The

101 accumulated macrophages were predominantly M $\varphi$ -A. We noted the absence of proliferation  
102 markers (*Cdk1*, *Ki67*) in this cluster, raising the possibility that this may be an infiltrative  
103 macrophage type (**Fig. 3d**). The M $\varphi$ -B cluster, located between M $\varphi$ -A and conventional  
104 dendritic cells (cDC) expressed also cDC markers such as MHC-II subunit genes (*H2-Ab1*) and  
105 *Cd11c* (*Itgax*) indicating that it is an intermediary macrophage type (**Fig. 3c**). This continuum  
106 between macrophages and dendritic cells in the kidney has been reported<sup>23-26</sup>. Interestingly,  
107 M $\varphi$ -B cells expressed proliferation markers (*Cdk1*, *Ki67*) and thus, may be differentiating  
108 towards a M $\varphi$ -A or cDC phenotype (**Fig. 3c**). Pseudotime and velocity field analysis suggested  
109 that at earlier time points (1 hour) M $\varphi$ -B was differentiating toward M $\varphi$ -A phenotype. At later  
110 time points (36 hours) the velocity field suggested that M $\varphi$ -B was differentiating towards cDC  
111 but pseudotime analysis was inconclusive (**Fig. 3e**). Similarly, the M $\varphi$ -A cluster also showed two  
112 subclusters on the RNA velocity map (**Supplementary Fig. 4a**). One of the subclusters showed  
113 increased expression of alternatively activated macrophages (M2) markers such as *Arg1*  
114 (Arginase 1) and *Mrc1* (*Cd206*)<sup>27</sup> at later time points (36 hours, **Supplementary Fig. 4b**).  
115 Therefore, RNA velocity analysis may be a useful tool in distinguishing macrophage subtypes in  
116 scRNAseq data.  
  
117 In T-cells, while *Cd4* expression was minimal at all time points, the expression of *Cd8* was  
118 robust and relatively preserved over time (**Fig. S4c**). We also noted an increase of a distinct  
119 plasmacytoid dendritic cell cluster at one hour (pDC). These pDCs, along with natural killer (NK)  
120 cells, are known to signal through the interferon-gamma pathway and stimulate Cd8 expression  
121<sup>28,29</sup>. This supports the early antiviral response we have previously reported in this sepsis model  
122<sup>5</sup>.  
  
123

124 *Cell trajectory and velocity field analyses of scRNAseq characterize subpopulations of epithelial  
125 and endothelial cells*

126 We next examined the phenotypic changes in various cell populations along the sepsis timeline.  
127 At each time point in sepsis, cells exhibited various states of gene expression that are well  
128 defined with pseudotime analysis. We note that at any given time point, directional progression  
129 of states along pseudotime correlated well with real time state changes (**Fig. 4a**). Note that the  
130 endothelium exhibited changes in states as early as 1 hour, while S1 showed changes at later  
131 time points (4 hours). These sequential state changes may reflect the spatial and temporal  
132 propagation of LPS signaling in the kidney. As sepsis progressed, many cell types lost function-  
133 defining markers while acquiring novel ones. For example, S1 and S3 lost classical markers like  
134 *Slc5a2* (SGLT2) and *Aqp1* and expressed new genes involved in antigen presentation such as  
135 *H2-Ab1* (MHC-II) and *Cd74* (**Fig. 4b**). Moreover, the highly distinct phenotypes that  
136 differentiated S1 from S2/S3 at baseline merged into one phenotype for all three sub-segments  
137 by 16 hours after LPS (**Fig. 4c**). However, despite the apparent convergent phenotype at 16  
138 hours, additional analytical approaches such as RNA velocity revealed significant differences in  
139 RNA splicing kinetics between S1 and S3 segments at this time point. In addition, RNA velocity  
140 revealed the presence of two subclusters within the S3 segment at 16 hours (**Fig. 4d**). These  
141 two velocity subclusters did not correlate with the two states seen in pseudotime analysis. This  
142 indicates that multiple analytic approaches are needed to fully characterize cellular changes  
143 along the sepsis timeline.

144 *Sepsis induces time and cell-specific genes and pathways*

145 We next show gene expression profiles in select cell types along the sepsis timeline. In this  
146 analysis, we included endothelial cells, pericyte/stromal cells, macrophages and S1 tubular  
147 cells. Within 1 hour of LPS exposure, most cell types showed decreased expression of select  
148 genes involved in ribosomal function, translation and mitochondrial processes such as *Eef2* and

149 *Rpl* genes (**Fig. 5a, Supplementary Fig. 5a**). This reduction peaked at 16 hours and recovered  
150 by 27 hours. Concomitantly, most cell types exhibited increased expression of several genes  
151 involved in inflammatory and antiviral responses such as *Tnfsf9*, *Cxcl1*, *Ifit1*, and *Irf7*. However,  
152 this increase was not synchronized among all cell populations. Indeed, it occurred as early as 1  
153 hour in endothelial cells, macrophages and pericyte/stromal cells, all acting as first responders.  
154 In contrast, epithelial cells were late responders, with increases in inflammatory and antiviral  
155 responses occurring between 4 and 16 hours. In fact, four hours after LPS administration,  
156 cluster-specific GO terms were indistinguishable among the majority of cell types with  
157 enrichment in terms related to defense, immune and bacterium responses (**Fig. 5b**). One noted  
158 exception was the S3T2 cells (outer stripe S3) which did not enrich as robustly as other cell  
159 types in these terms. It mostly maintained an expression profile related to ribosomes, translation  
160 and drug transport throughout the sepsis timeline (**Supplementary Fig. 6**). Other players of  
161 interest in sepsis pathophysiology such as prostaglandin and coagulation factors are described  
162 in **Supplementary Figure 5b**.

163 At the 48-hour time point, while S1 cells partially recovered to baseline, the macrophages  
164 showed increased expression of genes involved in phagocytosis, cell motility and leukotrienes,  
165 broadly representative of activated macrophages (e.g. *Csf1r*, *Lst1*, *Capzb*, *S100a4*, *Cotl1*,  
166 *Alox5ap*, **Fig. 5a**). Intriguingly, at this late time point, the pericyte/stromal cells are enriched in  
167 unique terms related to specific leukocyte and immune cell types such as lymphocyte-mediated  
168 immunity, T cell mediated cytotoxicity and antigen processing and presentation. This suggests  
169 that the pericyte may function as a transducer between epithelia and other immune cells.

170 *Sepsis alters cell-cell communication in the murine kidney*

171 Therefore, we next examined comprehensively cell-cell communication along the sepsis  
172 timeline. We show select examples of cell type-specific receptor ligand pairs. For example, we  
173 found that S1 and endothelial cells communicate with the *Angpt1* (Angiopoietin 1) and *Tek* (Tie2)

174 ligand-receptor pair at baseline and throughout the sepsis timeline (**Fig. 6a-b, Supplementary**

175 **Fig. 7a**). In contrast, C3 was strongly expressed in pericyte/stromal cells, while its receptor

176 C3ar1 localized to macrophage/DCs. This communication, present at baseline, did increase

177 along the sepsis timeline with additional players such as S1 participating in the cross talk

178 (**Supplementary Fig. 7**). Another strong communication was noted between endothelial cells

179 and macrophage/lymphocytes using the *Ccl2* and *Ccr2* receptor-ligand pair. The architectural

180 layout of these four cell types, with pericytes and endothelial cells residing between proximal

181 tubule and macrophage/DCs may explain these complex communication patterns<sup>6</sup>. Such

182 communication patterns among these four cell types may also explain macrophage clustering

183 around S1 tubules at later time points in sepsis as we previously reported<sup>13</sup>.

184 When examined comprehensively, receptor-ligand signaling progressed from a broad pattern at

185 baseline into a more discrete and specialized one 4 hours after LPS (**Fig. 6c, Supplementary**

186 **Fig. 7b-c**). Sixteen hours after LPS, we noted a dramatic drop in cell-cell communication

187 between all cell types. This communication failure may contribute to the transcription and

188 translation shutdown we recently reported at this time point<sup>5</sup>. In our reversible sepsis model,

189 cell-cell communication recovered by 27-48 hours.

190 *Sepsis induces time and cell-specific changes in regulons*

191 Transcription factors and their downstream targets (regulons) are important regulators of a

192 myriad of pathways involved in the pathophysiology of sepsis. Therefore, we next examined the

193 activity of regulons along the sepsis timeline in all renal cells. Surprisingly, we noted in many

194 cell types an increase in regulon activity of key transcription factors at the 16-hour time point

195 (**Supplementary Table 3**). As discussed above, this time point corresponds to translation

196 shutdown as well as cell-cell communication failure. In S1, many of the regulons active at this

197 time point are involved in cell differentiation, development, transcription and proliferation (*Sox4*,

198 *Hoxb7*, *Srf*, **Fig. 7a-c**). Therefore, this 16-hour time point is not merely a time of complete

199 shutdown and failure of the kidney. Rather, it is also a crucial transition point where key  
200 regulators of recovery and healing are being activated.

201 *The murine sepsis timeline allows staging of human sepsis*

202 Finally, we asked whether our mouse sepsis timeline could be used to stratify human sepsis  
203 AKI. To this end, we selected the differentially expressed genes from all cells combined (pseudo  
204 bulk) for each time point across the mouse sepsis timeline (**Supplementary Table 4**). We then  
205 examined the orthologues of these defining genes in human kidney biopsies of patients with  
206 sepsis and AKI. The clinical data associated with these human biopsies did not allow further  
207 stratification or staging of the sepsis timeline (**Supplementary Table 5**). As shown in **Figure 7d**,  
208 our approach using the mouse data succeeded in partially stratifying the human biopsies into  
209 early, mid and late sepsis-related AKI. These findings suggest that underlying injury  
210 mechanisms are conserved, and the mouse timeline may be valuable in staging and defining  
211 biomarkers and therapeutics in human sepsis.

212 **Discussion**

213 In this work, we provide comprehensive transcriptomic profiling of the kidney in a murine sepsis  
214 model. To our knowledge, this is the first description of spatial and temporal transcriptomic  
215 changes in the septic kidney that extend from early injury well into the recovery phase. Our data  
216 cover nearly all renal cell types and are time-anchored, thus providing a detailed and precise  
217 view of the evolution of sepsis in the kidney at the cellular and molecular level.

218 Using a combination of analytical approaches, we identified marked phenotypic changes in  
219 multiple cell populations along the sepsis timeline. The proximal tubular S1 segment exhibited  
220 significant alterations consisting of early loss of traditional function-defining markers (e.g.,  
221 SGLT2). Similar losses of function-defining markers along the nephron may explain the  
222 profound derangement in solute and fluid homeostasis seen in sepsis. Concomitantly, we

223 observed novel epithelial expression of immune-related genes such as those involved in antigen  
224 presentation. This indicates a dramatic switch in epithelial function from transport and  
225 homeostasis to immunity and defense. These phenotypic changes were reversible, thus  
226 underscoring the remarkable resilience and plasticity of the renal epithelium.

227 In addition, our combined analytical tools clearly identified unique subclusters within each  
228 epithelial cell population (e.g., cortical S3 and OS S3). These subclusters likely represent novel  
229 populations that may be in part influenced by the complex microenvironments in the kidney. It is  
230 likely that such microenvironments define unique features in epithelial subpopulations such as  
231 the expression of complete SARS-CoV-2 machinery in S1.

232 Similarly, we also identified unique features in immune-cell populations. For example, the  
233 combined use of RNA velocity field and pseudotime analyses uncovered differences in  
234 macrophage subtypes relating to RNA kinetics and cell differentiation trajectories. Of note is that  
235 these subtypes only partially matched the traditional flow cytometry-based classification of  
236 macrophages (e.g., M1/M2). Therefore, the use of single-cell RNA seq is a powerful approach  
237 that will add to and complement our current understanding of the immune cell repertoire in the  
238 kidney.

239 Additional approaches such as receptor-ligand crosstalk and gene regulatory network analyses  
240 identified unique cell- and time-dependent players involved in sepsis pathophysiology.

241 Importantly, the expression of genes involved in vectorial transport, inflammation, vascular  
242 health and cell-cell communication varied greatly along the sepsis timeline, and required  
243 simultaneous contributions from multiple cell types. However, these complex interactions  
244 collapsed at the 16-hour time point. This indeed is a remarkable time in the sepsis timeline that  
245 we have previously investigated in multiple models of murine sepsis. It is the time where  
246 profound translation failure and organ shutdown occur. Our current data point to massive cell-  
247 cell communication failure as a key feature of this time point. Surprisingly, it is also at this time

248 point that reparative pathways started to emerge. It is thus an important and defining point in  
249 sepsis that may have significant clinical implications.

250 Our work points to the urgent need for defining a more accurate and precise timeline for human  
251 sepsis. Such definition will guide the development of biomarkers and therapies that are cell and  
252 time specific. We show evidence supporting the relevance of murine models and their  
253 usefulness in staging human sepsis. These precisely time- and space-anchored data will  
254 provide the community with rich and comprehensive foundations that will propel further  
255 investigations into human sepsis.

256 **Methods**

257 ***Experimental Model and Subject Details***

258 *Animal model:* Male C57BL/6J mice were obtained from the Jackson Laboratory. Mice were 8-  
259 10 weeks of age and weighed 20-25 g. They were subjected to a single dose of 5 mg/kg LPS  
260 tail vein injection (*E. coli* serotype 0111:B4 Sigma). Animals were sacrificed at 0, 1, 4, 16, 27, 36  
261 and 48 hours after LPS (both kidneys per animal for each time point). For spatial  
262 transcriptomics experiments, cecal ligation and puncture (CLP) was performed under isoflurane  
263 anesthesia; 75% of the mouse cecum was ligated and punctured twice with a 27-gauge needle  
264 and the mouse sacrificed and kidneys harvested 6 hours later.

265 *Study approval:* All animal protocols were approved by the Indiana University Institutional  
266 Animal Care Committee and conform to the NIH (*Guide for the Care and Use of Laboratory*  
267 *Animals*, National Academies Press, 2011). The study in humans was approved by the Indiana  
268 University Institutional Review Board (protocol no. 1601431846). As only archived human  
269 biopsies were used in this study, the Institutional Review Board determined that informed  
270 consent was not required.

271

272 ***Isolation of single cell homogenate from murine kidneys***

273 Murine kidneys were transported in RPMI1640 (Corning), on ice immediately after surgical  
274 procurement. Kidneys were rinsed with PBS (ThermoFisher) and minced into eight sections.  
275 Each sample was then enzymatically and mechanically digested with reagents from Multi-  
276 Tissue Dissociation Kit 2 and GentleMACS dissociator/tube rotator (Miltenyi Biotec). The  
277 samples were prepared per protocol “Dissociation of mouse kidney using the Multi Tissue  
278 Dissociation Kit 2” with the following modifications: After termination of the program “Multi\_E\_2”,  
279 we added 10 mL RPMI1640 (Corning) and 10% BSA (Sigma-Aldrich) to the mixture, filtered and  
280 homogenate was centrifuged (300 g for 5 minutes at 4°C). Cell pellet was resuspended in 1 mL  
281 of RBC lysis buffer (Sigma), incubated on ice for 3 minutes, and cell pellet washed three times  
282 (300 g for 5 minutes at 4°C ). Annexin V dead cell removal was performed using magnetic bead  
283 separation after final wash, and the pellet resuspended in RPMI1640/BSA 0.04%. Viability and  
284 counts were assessed using Trypan blue (Gibco) and brought to a final concentration of 1  
285 million cells/mL, exceeding 80% viability as specified by 10x Genomics processing platform.

286

287 ***Single cell library preparation***

288 The sample was targeted to 10,000 cell recovery and applied to a single cell master mix with  
289 lysis buffer and reverse transcription reagents, following the Chromium Single Cell 3' Reagent  
290 Kits V3 User Guide, CG000183 Rev A (10X Genomics, Inc.). This was followed by cDNA  
291 synthesis and library preparation. All libraries were sequenced in Illumina NovaSeq6000  
292 platform in paired-end mode (28bp + 91bp). Fifty thousand reads per cell were generated and  
293 91% of the sequencing reads reached Q30 (99.9% base call accuracy). The total number of  
294 recovered cells for all time points was 63,287 cells, and per experiment was 9,191 (0 hour),  
295 9,460 (1 hour), 9,865 (4 hours), 5,165 (16 hours), 7,678 (27 hours), 10,119 (36 hours), and  
296 11,809 (48 hours after LPS).

297

298

299 ***Single cell data processing***

300 The 10x Genomics Cellranger (v. 2.1.0) pipeline was utilized to demultiplex raw base call files to  
301 FASTQ files and reads aligned to the mm10 murine genome using STAR<sup>30</sup>. Cellranger  
302 computational output was then analyzed in R (v.3.5.0) using the Seurat package v. 3.0.0.9999,  
303<sup>31</sup>. Seurat objects were created for non-integrated and integrated (inclusive of all time points)  
304 using the following filtering metrics: gene counts were set between 200-3000 and mitochondrial  
305 gene percentages less than 50 to exclude doublets and poor quality cells. Gene counts were log  
306 transformed and scaled to 10<sup>4</sup>. The top 20 principle components were used to perform  
307 unsupervised clustering analysis, and visualized using UMAP dimensionality reduction  
308 (resolution 1.0). Using the Seurat package, annotation and grouping of clusters to cell type was  
309 performed manually by inspection of differentially expressed genes (DEGs) for each cluster,  
310 based on canonical marker genes in the literature<sup>8-10,32,33</sup>. In some experiments, we used  
311 edgeR negative binomial regression to model gene counts and performed differential gene  
312 expression and pathway enrichment analyses (topKEGG, topGO, **Fig. 5, Supplementary Fig.**  
313 **5a, Supplementary Fig. 6**, and DAVID 6.8 **Fig. 7b**).<sup>34,35</sup>

314 The immune cell subset was derived from the filtered, integrated Seurat object and included the  
315 Macrophage/DC (cluster 10), neutrophil (cluster 19) and lymphocyte (cluster 13) cells. Gene  
316 counts were log transformed, scaled and principle component analysis performed as for the  
317 integrated object above. UMAP resolution was set to 0.4, which yielded 14 clusters. The  
318 clusters were manually assigned based on inspection of DEGs for each cluster, and cells  
319 grouped if canonical markers were biologically redundant. We confirmed manual labeling with  
320 an automated labeling program in R, SingleR<sup>36</sup>.

321 ***Analysis of regulons and their activity in the integrated single cell dataset***

322 SCENIC analysis<sup>37</sup> was performed using the default setting and mm9-500bp-upstream-  
323 7species.mc9nr.feather database was used for data display.

324 ***Pseudotemporal ordering of single cells***

325 We performed pseudotime analysis on the integrated Seurat object containing all cell types as  
326 well as the immune cell subset. Cells from each of the seven time points were included and  
327 were split into individual gene expression data files organized by previously defined cell type.  
328 These individual datasets were analyzed separately through the R package Monocle using  
329 default parameters. Outputs were obtained detailing the pseudotime cell distributions for each  
330 cell type. Positional information for the monocle plot was used to subset and color cells for  
331 downstream analyses<sup>38</sup>. We performed a separate temporal ordering analysis of S1, S2 and  
332 S3 proximal tubule segments across all time points and visualized using t-SNE, produced by  
333 Harmony and Palantir R packages<sup>39</sup>.

334 ***RNA velocity analysis***

335 BAM files were fed through the velocyto pipeline<sup>40</sup> to obtain .loom files for each experimental  
336 condition. These loom files along with their associated UMAP positions and principal component  
337 tables extracted from the merged Seurat file were then fed individually into the RNA Velocity  
338 pipeline as described in the Velocyto.R Dentate Gyrus/loom tutorial. The default settings  
339 described in the tutorial were used except for tSNE positions that were overwritten with the  
340 associated UMAP positions from the merged Seurat object, as well as the principal component  
341 table. This generated an RNA velocity Fig. mapped using the merged Seurat object cell  
342 positions. Similar analysis was done for the immune subsetted data.

343 ***Cell-cell communication analysis***

344 We applied the Cellphone database<sup>41</sup> of known receptor-ligand pairs to assess cell-cell  
345 communication in our integrated dataset. Gene expression data from the integrated Seurat file

346 was split by time point and genes renamed to Human gene names then reformatted into the  
347 input format described on the CellphoneDB website. Individual time point samples were fed into  
348 the web document on the cellphone dB website using 50 iterations, precision of 3, and 0.1 ratio  
349 of cells in a cluster expressing a gene. Output files for each time point obtained from the  
350 website were merged, then interactions trimmed based on significant sites and only selecting  
351 secreted interactions.

352 To visualize cellular cross talk, we applied this data to a circular plot. The interactions from the  
353 merged, trimmed cellphone dB file were sorted by cluster interaction then consolidated into 17  
354 final cell types. Each cell type contained a list of significant interacting pairs (with  $p < 0.05$ ) and  
355 their associated strength values (the larger the value the smaller the  $p$  value). These were then  
356 visualized using R Circlize package<sup>42</sup>

357 ***Human sepsis staging***

358 Murine scRNAseq data was pseudobulked though selection of 2000 randomly selected cells for  
359 each of seven time points and data normalized using edgeR function calcNormFactors. DEGs  
360 were found between one versus rest of time points and significant genes filtered by selecting for  
361 FDR  $<0.05$ . Human specimens were derived from OCT cores of kidney biopsy or nephrectomy  
362 samples (GSE139061). All biopsy specimens ( $N = 22$ ) had a primary pathology diagnosis of AKI  
363 and were acquired in clinical care of patients with a diagnosis of sepsis<sup>5</sup>. The reference  
364 nephrectomies were obtained from unaffected portions of tumor nephrectomies or deceased  
365 donors. A bulk 20- $\mu\text{m}$  cross-section was cut from each OCT core and RNA was extracted using  
366 the Arcturus Picopure extraction kit (KIT0214, Thermo Fisher Scientific, Waltham, MA). Libraries  
367 were prepared with the Takara SMARTer® Stranded Total RNA-Seq Kit v2 - Pico Input.  
368 Sequencing was performed on an Illumina HiSeq 4000. The murine genes from each  
369 pseudobulk time point were translated to their respective human orthologues using the biomaRt  
370 package and ensembl database. Each gene had its expression fold change calculated for each

371 time point in relation to all other time points in the mouse. Separately for each human biopsy  
372 specimen, the expression of each gene was calculated as a fold change compared to the mean  
373 of all reference samples. A spearman correlation assessed alignment between the fold  
374 changes of the mouse and human data. Data were displayed as a heatmap.

375 ***Spatial Transcriptomics***

376 A septic mouse kidney was immediately frozen in Optimal Cutting Temperature media. A 10 µm  
377 frozen tissue section was cut and affixed to a Visium Spatial Gene Expression library  
378 preparation slide (10X Genomics). The specimen was fixed in methanol and stained with  
379 hematoxylin-eosin reagents. Images of hematoxylin-eosin-labeled tissues were collected as  
380 mosaics of 10x fields using a Keyence BZ-X810 fluorescence microscope equipped with a  
381 Nikon 10X CFI Plan Fluor objective. The tissue was then permeabilized for 12 minutes and RNA  
382 was isolated. The cDNA libraries were prepared and then sequenced on an Illumina NovaSeq  
383 6000. Using Seurat 3.1.4, we identified anchors between the integrated single cell object and  
384 the spatial transcriptomics datasets and used those to transfer the cluster data from the single  
385 cell to the spatial transcriptomics. For each spatial transcriptomics spot, this transfer assigns a  
386 score to each single cell cluster. We selected the cluster with the highest score in each spot to  
387 represent its single cell associated cluster. Using a Loupe Browser, expression data was  
388 visualized overlying the hematoxylin-eosin image.

389 ***Single-molecule RNA in situ hybridization***

390 Formalin-fixed paraffin-embedded cross sections were prepared with a thickness of 5µm. The  
391 slides were baked for 60 minutes at 60 °C. Tissues were incubated with Xylene for 5 minutes  
392 x2, 100% ETOH for 2 minutes x2, and dried at room temperature. RNA in situ hybridization was  
393 performed using RNAscope multiplex Fluorescent Reagent Kit v2 (Advance Cell Diagnosis Inc.)  
394 as per the manufacturer instructions. Probe sets were obtained from Advance Cell Diagnosis

395 Inc (murine Agt Cat. No. 426941, Aqp1 Cat. No. 504741-C2). TSA Cyanine 3 Plus and  
396 Fluorescein Plus Evaluation kit (PerkinElmer, Inc) was used as secondary probes for the  
397 detection of RNA signals. All slides were counterstained with DAPI and coverslips were  
398 mounted using fluorescent mounting media (ProLong Gold Antifade Reagent, Life  
399 Technologies). The images were collected with a LSM800 confocal microscope (Carl Zeiss).

400 ***Quantification and Statistical Analysis***

401 No blinding was used for animal experiments. All data were analyzed using R software  
402 packages, with relevant statistics described in results, methods and Fig. legends.

403 ***Data availability***

404 Data will be deposited to NCBI GEO. The authors declare that all relevant data supporting the  
405 findings of this study are available on request.

406 ***Code availability***

407 R scripts for performing the main steps of analysis are available from the Lead contact on  
408 request.

409 ***Additional Information***

410 Correspondence and requests for resources and reagents should be directed to and will be  
411 fulfilled by the Lead Contact Takashi Hato ([thato@iu.edu](mailto:thato@iu.edu)).

412

413 ***Supplemental items***

414 Supplemental Fig. 1-7: refer to “Supplemental\_Fig 1-7.pdf”

415 Supplemental Table 1: Cell-type specific differentially expressed genes from 0-48 hours, related  
416 to Fig. 1, Supplemental Fig. 1.

417      Supplemental Table 2: Numbered interactions of receptor ligand interactions between cell type  
418      pairs, related to Fig. 6 and Supplemental Fig. 7.  
  
419      Supplemental Table 3: Scenic regulatory gene network analysis of select cell types highlighting  
420      upregulated genes from 16-hour time point, related to Fig. 7.  
  
421      Supplemental Table 4: Murine pseudo bulked genes and counts from 0-48 hours, related to Fig.  
422      7.  
  
423      Supplemental Table 5: Human gene count matrices and clinical data from AKI renal biopsies,  
424      related to Fig. 7.  
  
425  
  
426  
  
427  
  
428  
  
429  
  
430  
  
431  
  
432  
  
433  
  
434  
  
435  
  
436  
  
437  
  
438

439 **References:**

- 440 1. Husain-Syed, F., Slutsky, A.S. & Ronco, C. Lung-Kidney Cross-Talk in the Critically Ill Patient. *Am J  
441 Respir Crit Care Med* **194**, 402-414 (2016).
- 442 2. Lee, S.A., Cozzi, M., Bush, E.L. & Rabb, H. Distant Organ Dysfunction in Acute Kidney Injury: A  
443 Review. *Am J Kidney Dis* **72**, 846-856 (2018).
- 444 3. Deutschman, C.S. & Tracey, K.J. Sepsis: current dogma and new perspectives. *Immunity* **40**, 463-  
445 475 (2014).
- 446 4. Poston, J.T. & Koyner, J.L. Sepsis associated acute kidney injury. *BMJ* **364**, k4891 (2019).
- 447 5. Hato, T., et al. Bacterial sepsis triggers an antiviral response that causes translation shutdown. *J  
448 Clin Invest* **129**, 296-309 (2019).
- 449 6. Wu, H., Kirita, Y., Donnelly, E.L. & Humphreys, B.D. Advantages of Single-Nucleus over Single-Cell  
450 RNA Sequencing of Adult Kidney: Rare Cell Types and Novel Cell States Revealed in Fibrosis. *J Am  
451 Soc Nephrol* **30**, 23-32 (2019).
- 452 7. Clark, J.Z., et al. Representation and relative abundance of cell-type selective markers in whole-  
453 kidney RNA-Seq data. *Kidney Int* **95**, 787-796 (2019).
- 454 8. Lake, B.B., et al. A single-nucleus RNA-sequencing pipeline to decipher the molecular anatomy  
455 and pathophysiology of human kidneys. *Nat Commun* **10**, 2832 (2019).
- 456 9. Lee, J.W., Chou, C.L. & Knepper, M.A. Deep Sequencing in Microdissected Renal Tubules  
457 Identifies Nephron Segment-Specific Transcriptomes. *J Am Soc Nephrol* **26**, 2669-2677 (2015).
- 458 10. Park, J., et al. Single-cell transcriptomics of the mouse kidney reveals potential cellular targets of  
459 kidney disease. *Science (New York, N.Y.)* **360**, 758-763 (2018).
- 460 11. Ransick, A., et al. Single-Cell Profiling Reveals Sex, Lineage, and Regional Diversity in the Mouse  
461 Kidney. *Dev Cell* **51**, 399-413 e397 (2019).
- 462 12. Hato, T., et al. The macrophage mediates the renoprotective effects of endotoxin  
463 preconditioning. *J Am Soc Nephrol* **26**, 1347-1362 (2015).
- 464 13. Hato, T., et al. Endotoxin Preconditioning Reprograms S1 Tubules and Macrophages to Protect  
465 the Kidney. *J Am Soc Nephrol* **29**, 104-117 (2018).
- 466 14. Kalakeche, R., et al. Endotoxin uptake by S1 proximal tubular segment causes oxidative stress in  
467 the downstream S2 segment. *J Am Soc Nephrol* **22**, 1505-1516 (2011).
- 468 15. Yang, L., Besschetnova, T.Y., Brooks, C.R., Shah, J.V. & Bonventre, J.V. Epithelial cell cycle arrest  
469 in G2/M mediates kidney fibrosis after injury. *Nat Med* **16**, 535-543, 531p following 143 (2010).
- 470 16. Cao, J., et al. Joint profiling of chromatin accessibility and gene expression in thousands of single  
471 cells. *Science (New York, N.Y.)* **361**, 1380-1385 (2018).
- 472 17. Stahl, P.L., et al. Visualization and analysis of gene expression in tissue sections by spatial  
473 transcriptomics. *Science (New York, N.Y.)* **353**, 78-82 (2016).
- 474 18. Yan, R., et al. Structural basis for the recognition of SARS-CoV-2 by full-length human ACE2.  
475 *Science (New York, N.Y.)* **367**, 1444-1448 (2020).
- 476 19. Hoffmann, M., et al. SARS-CoV-2 Cell Entry Depends on ACE2 and TMPRSS2 and Is Blocked by a  
477 Clinically Proven Protease Inhibitor. *Cell* **181**, 271-280 e278 (2020).
- 478 20. Puelles, V.G., et al. Multiorgan and Renal Tropism of SARS-CoV-2. *N Engl J Med* (2020).
- 479 21. Su, H., et al. Renal histopathological analysis of 26 postmortem findings of patients with COVID-  
480 19 in China. *Kidney Int* (2020).
- 481 22. Sungnak, W., et al. SARS-CoV-2 entry factors are highly expressed in nasal epithelial cells  
482 together with innate immune genes. *Nat Med* **26**, 681-687 (2020).
- 483 23. Kruger, T., et al. Identification and functional characterization of dendritic cells in the healthy  
484 murine kidney and in experimental glomerulonephritis. *J Am Soc Nephrol* **15**, 613-621 (2004).

- 485 24. Waltman, A.M., et al. Quantification of dendritic cell subsets in human renal tissue under  
486 normal and pathological conditions. *Kidney Int* **71**, 1001-1008 (2007).
- 487 25. Huen, S.C. & Cantley, L.G. Macrophages in Renal Injury and Repair. *Annu Rev Physiol* **79**, 449-469  
488 (2017).
- 489 26. Gottschalk, C. & Kurts, C. The Debate about Dendritic Cells and Macrophages in the Kidney.  
490 *Front Immunol* **6**, 435 (2015).
- 491 27. Lee, S., et al. Distinct macrophage phenotypes contribute to kidney injury and repair. *J Am Soc  
492 Nephrol* **22**, 317-326 (2011).
- 493 28. Guillerey, C., et al. Pivotal role of plasmacytoid dendritic cells in inflammation and NK-cell  
494 responses after TLR9 triggering in mice. *Blood* **120**, 90-99 (2012).
- 495 29. Hemann, E.A., et al. Interferon-lambda modulates dendritic cells to facilitate T cell immunity  
496 during infection with influenza A virus. *Nat Immunol* **20**, 1035-1045 (2019).
- 497 30. Dobin, A., et al. STAR: ultrafast universal RNA-seq aligner. *Bioinformatics (Oxford, England)* **29**,  
498 15-21 (2013).
- 499 31. Stuart, T., et al. Comprehensive Integration of Single-Cell Data. *Cell* **177**, 1888-1902.e1821  
500 (2019).
- 501 32. Kretzler, M. & Ju, W. A Transcriptional Map of the Renal Tubule: Linking Structure to Function. *J  
502 Am Soc Nephrol* **26**, 2603-2605 (2015).
- 503 33. Wu, H., et al. Single-Cell Transcriptomics of a Human Kidney Allograft Biopsy Specimen Defines a  
504 Diverse Inflammatory Response. *J Am Soc Nephrol* **29**, 2069-2080 (2018).
- 505 34. Alessandri, L., Arigoni, M. & Calogero, R. Differential Expression Analysis in Single-Cell  
506 Transcriptomics. *Methods Mol Biol* **1979**, 425-432 (2019).
- 507 35. Huang da, W., Sherman, B.T. & Lempicki, R.A. Bioinformatics enrichment tools: paths toward the  
508 comprehensive functional analysis of large gene lists. *Nucleic Acids Res* **37**, 1-13 (2009).
- 509 36. Aran, D., et al. Reference-based analysis of lung single-cell sequencing reveals a transitional  
510 profibrotic macrophage. *Nat Immunol* **20**, 163-172 (2019).
- 511 37. Aibar, S., et al. SCENIC: single-cell regulatory network inference and clustering. *Nat Methods* **14**,  
512 1083-1086 (2017).
- 513 38. Trapnell, C., et al. The dynamics and regulators of cell fate decisions are revealed by  
514 pseudotemporal ordering of single cells. *Nature biotechnology* **32**, 381-386 (2014).
- 515 39. Setty, M., et al. Characterization of cell fate probabilities in single-cell data with Palantir. *Nature  
516 biotechnology* **37**, 451-460 (2019).
- 517 40. La Manno, G., et al. RNA velocity of single cells. *Nature* **560**, 494-498 (2018).
- 518 41. Efremova, M., Vento-Tormo, M., Teichmann, S.A. & Vento-Tormo, R. CellPhoneDB: inferring cell-  
519 cell communication from combined expression of multi-subunit ligand-receptor complexes. *Nat  
520 Protoc* **15**, 1484-1506 (2020).
- 521 42. Gu, Z., Gu, L., Eils, R., Schlesner, M. & Brors, B. circlize Implements and enhances circular  
522 visualization in R. *Bioinformatics (Oxford, England)* **30**, 2811-2812 (2014).

523

524

525

526

527 **Acknowledgements:**

528 We thank the Kidney Precision Medicine Project for making data available for human kidney  
529 reference nephrectomy specimens. We thank Daria Barwinska for assistance with specimen  
530 validation. This work was supported by NIH K08-DK113223 to TH, NIH R01-DK080063,  
531 Veterans Affairs Merit (1I01BX002901) and the Indiana Clinical and Translational Sciences  
532 Institute (UL1TR002529) to PCD, K08-DK107864 to MTE, T32HL091816 and T32DK120524 to  
533 DJ.

534 **Author contributions:**

535 Conceptualization DJ, PCD and TH. scRNAseq Methodology DJ, BM, PCD and TH. scRNAseq  
536 Software, formal analysis, visualization TH, JM, DJ. Investigation DJ, AZ, TH. Validation KC and  
537 SW, TA. Resources for single cell data, spatial transcriptomics, and human data TH, PD, TA,  
538 MTE, RMF. Data curation, DJ, TH, TWM, JM. Writing- original draft, DJ, PD, TH. Supervision,  
539 TH and PD. Funding PD, TH, DJ.

540

541

542

543

544

545

546

547

548

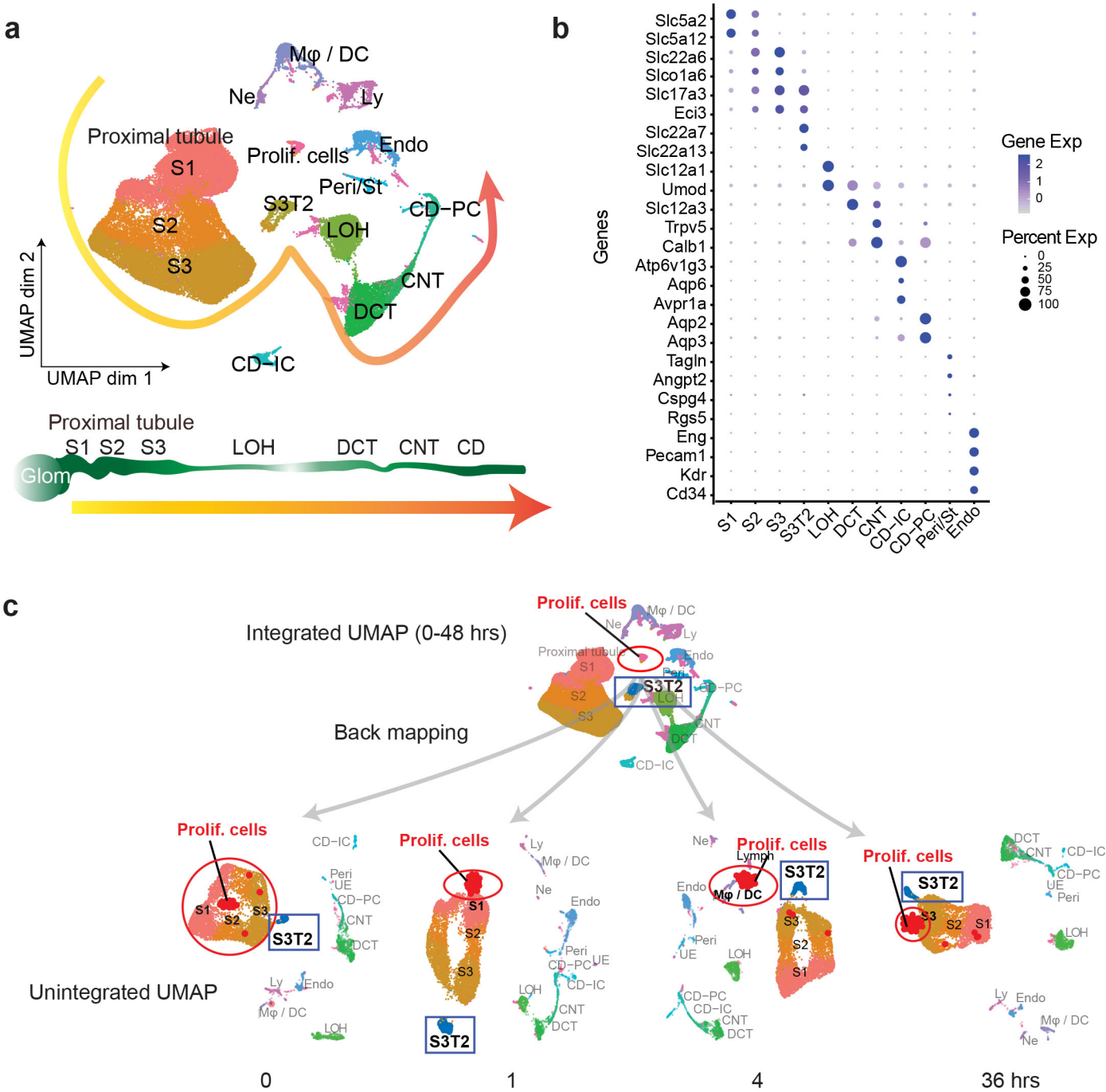
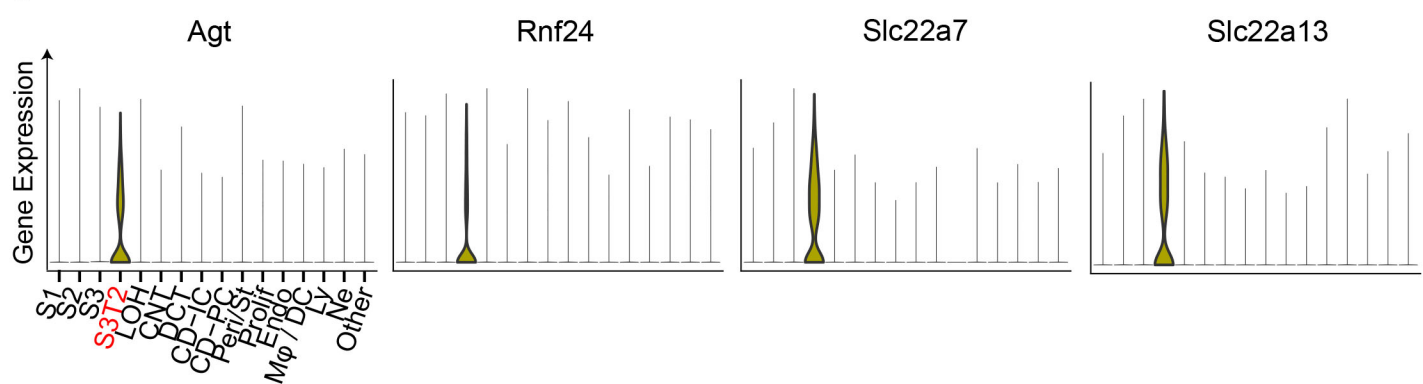


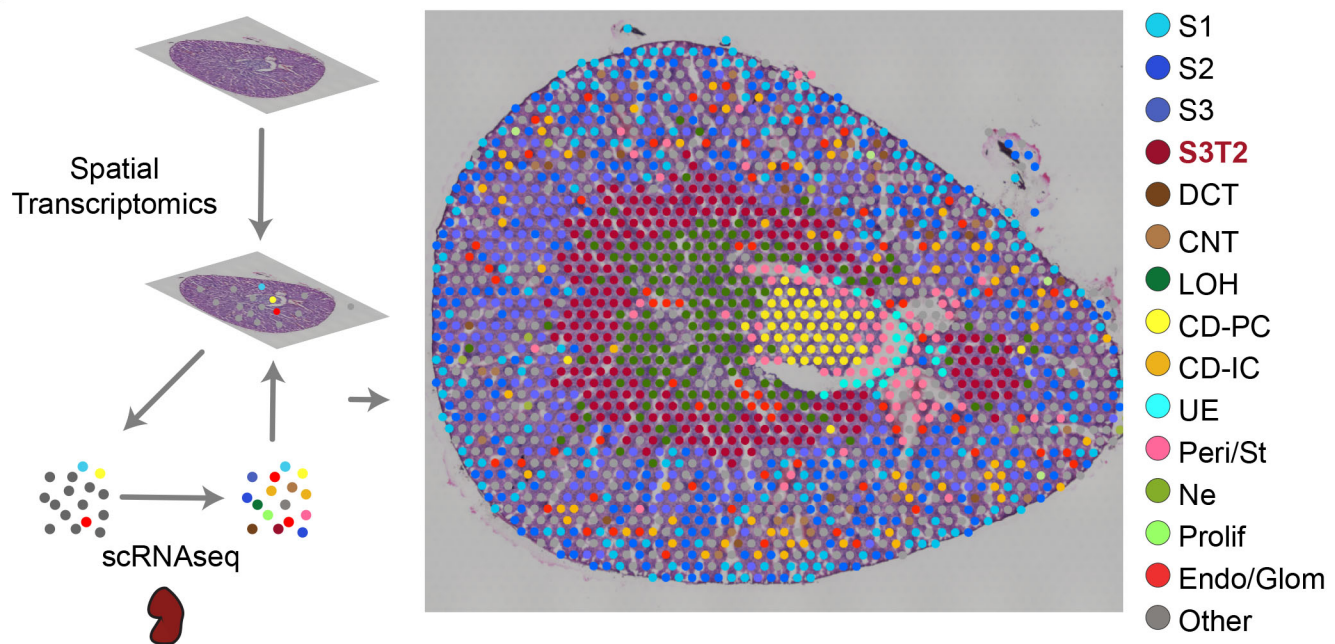
**Fig. 1: Single cell RNA sequencing identifies renal epithelial, endothelial, stromal and immune cell types in the murine septic kidney**

**a** Integrated UMAP of kidney cell clusters from control and LPS-treated mice (0, 1, 4, 16, 27, 36 and 48 hours after LPS injection). Actual anatomical layout of kidney nephronal segments is shown below UMAP. **b** Dot plot of representative genes defining indicated cell types. **c** Back mapping of cells from the integrated UMAP onto unintegrated UMAPs of select time points. Highlighted are the proliferating cell cluster (red circle) and S3T2 cluster (blue box). CD, collecting duct. CD-IC, collecting duct-intercalated cells. CD-PC, collecting duct-principle cells. CNT, connecting tubule. DCT, distal convoluted tubule. Endo, endothelial cells. Exp, expression. Glom, glomerulus. LOH, Loop of Henle. LPS, endotoxin. Ly, lymphocytes. Mφ-DC, macrophage-dendritic cells. Ne, neutrophil. Peri/St, mixed pericyte and stromal cells. Prolif. Cells, proliferative cells. PT, proximal tubule. S1, first segment of PT. S2, second segment of PT. S3, third segment of PT. S3T2, S3 type 2 cells.

a



b



c

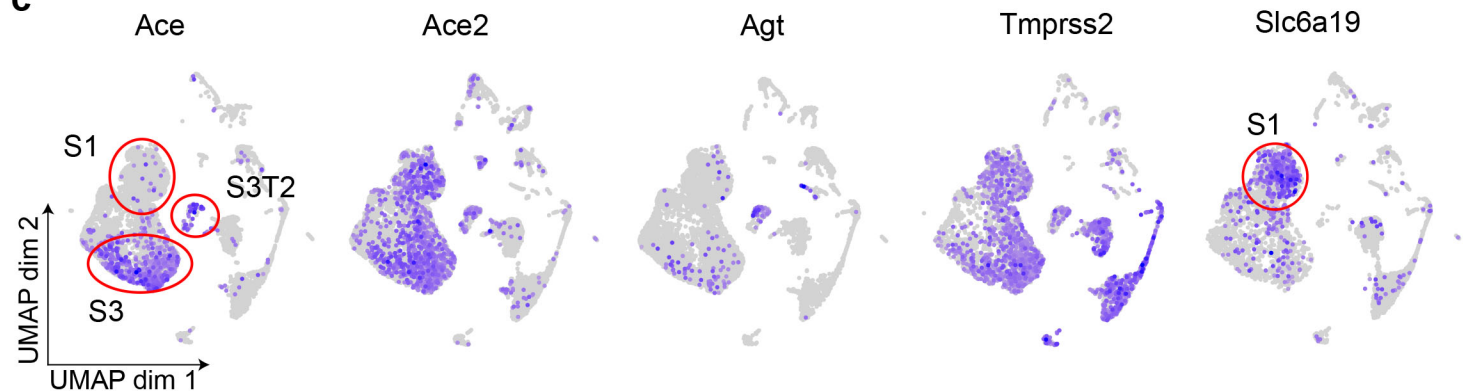


**Fig. 2: Spatial transcriptomics localize S3- Type 2 cells to the outer stripe of the outer medulla.** **a** Violin plots of S3T2 defining markers. **b** Integration of spatial transcriptomics and scRNASeq. Spatial transcriptomics were performed on a slice of mouse kidney after cecal ligation and puncture. This yielded 7 clusters that were expanded to 15 cell types by integrating spatial transcriptomics with scRNASeq data from LPS-treated mice. See also **Supplemental Fig. 2b**. **c** Feature plots of select renin-angiotensin system and other SARS-CoV-2-related genes. See also **Supplemental Fig. 3**. CD, collecting duct. CD-IC, collecting duct-intercalated cells. CD-PC, collecting duct-principle cells. CNT, connecting tubule. DCT, distal convoluted tubule. Endo, endothelial cells. Exp, expression. Glom, glomerulus. Hrs, hours. LOH, Loop of Henle. Ly, lymphocytes. Mφ-DC, macrophage-dendritic cells. Ne, neutrophil. Peri/St, mixed pericyte and stromal cells. Prolif., proliferative cells. PT, proximal tubule. S1, first segment of PT. S2, second segment of PT. S3, third segment of PT. S3T2, S3 type 2 cells. scRNASeq, single cell RNA sequencing.

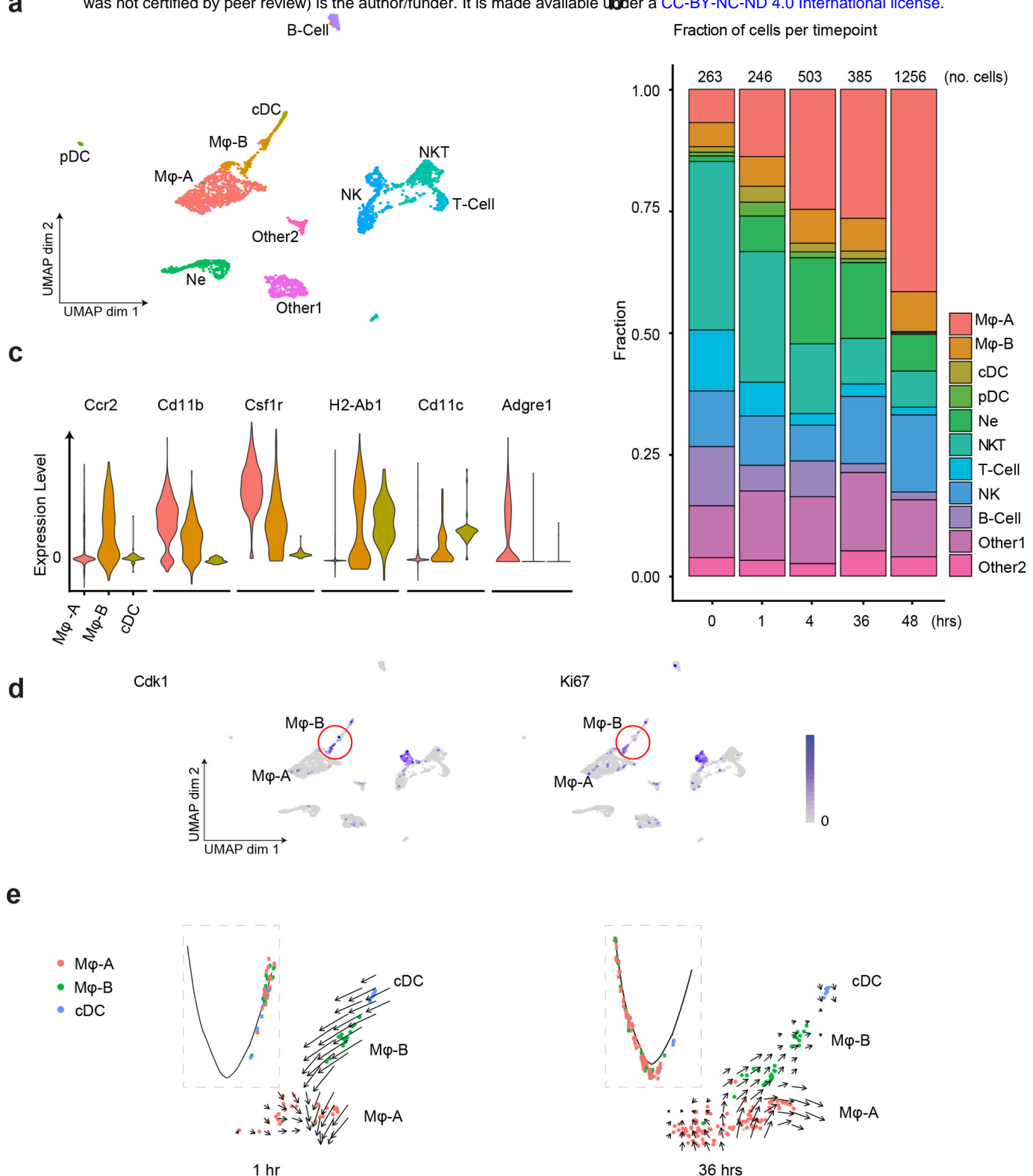


**Fig. 3: Sepsis induces dynamic changes in renal immune cell composition, pseudotime states and RNA velocity. a** Integrated UMAP of the immune cell clusters from control and LPS-treated mice (0, 1, 4, 16, 27, 36 and 48 hours after LPS injection). Other 1 and Other 2 are Cd45+ cells with mixed epithelial and immune markers. **b** Stacked bar plot with fractions of immune cells (relative to total number of cells) shown in the y-axis, at 0, 1, 4, 36 and 48 hours after LPS. The total number of immune cells is indicated at the top of the bar for each time point. **c** Integrated violin plots from all time points for indicated genes defining subtypes of macrophages and DCs are shown. **d** Feature plots of proliferation markers expression from integrated time points in the immune cell subsets. **e** Integrated cell trajectory analyses and RNA velocity fields for macrophages and dendritic cells shown at indicated time points. cDC, conventional dendritic cell. Hrs, hours. Mφ-A, macrophage-A. Mφ-B, macrophage-B. Ne, neutrophil. NK, natural killer cells. NKT, natural killer T-cells. pDC, plasmacytoid dendritic cell. T-cell, Cd3+ T-lymphocytes.

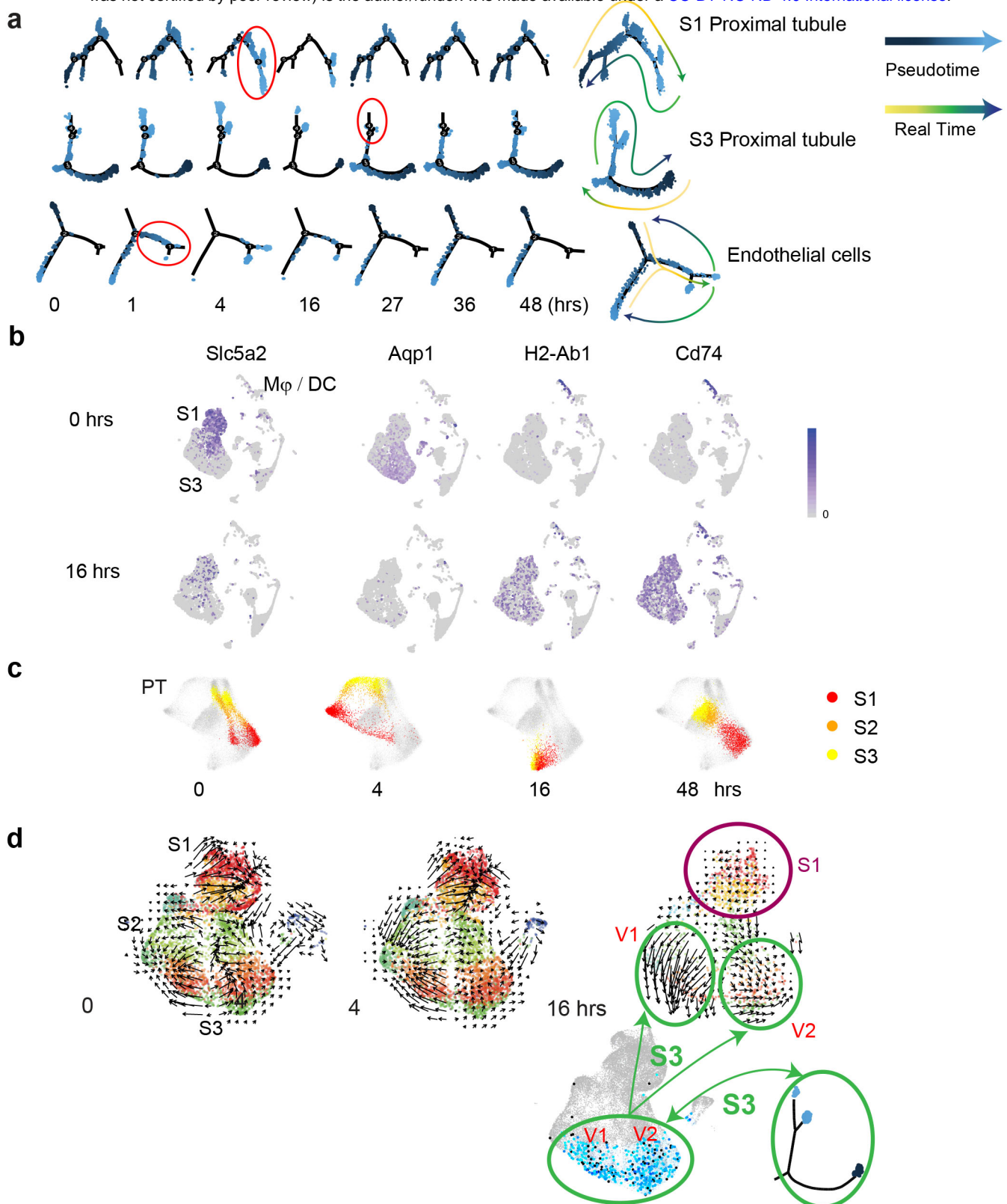


**Fig. 4: Sepsis alters pseudotime states, phenotypic gene expression and RNA velocity in renal cell populations.** **a** Cell trajectory analysis for S1, S3 and endothelial cells shown at indicated time points. Highlighted in red circles are significant state transitions in respective cell types. The last cell trajectory shown for each cell type is integrated from all time points. It highlights the correspondence between pseudotime and real time. **b** Feature plots of select genes shown at indicated time points highlighting proximal tubular phenotypic changes. **c** Time-specific S1, S2 and S3 PT cells (red, orange, yellow) overlaid on composite t-SNE map of all PT cells (grey). **d** RNA velocity fields for S1, S2, and S3 proximal tubular cells are shown at indicated time points. Two velocity subfields V1 and V2 in S3 cells are circled in green. Projections of two pseudotime S3 states (light blue, dark blue dots) onto the S3 velocity fields do not show a 1:1 correspondence with the two velocity subfields V1 and V2. Hrs, hours. M $\phi$ -DC, macrophage-dendritic cells. Ne, neutrophil. PT, proximal tubule. S1, first segment of PT. S2, second segment of PT. S3, third segment of PT. S3T2, S3 type 2 cells. V1, velocity subfield 1. V2, velocity subfield 2.

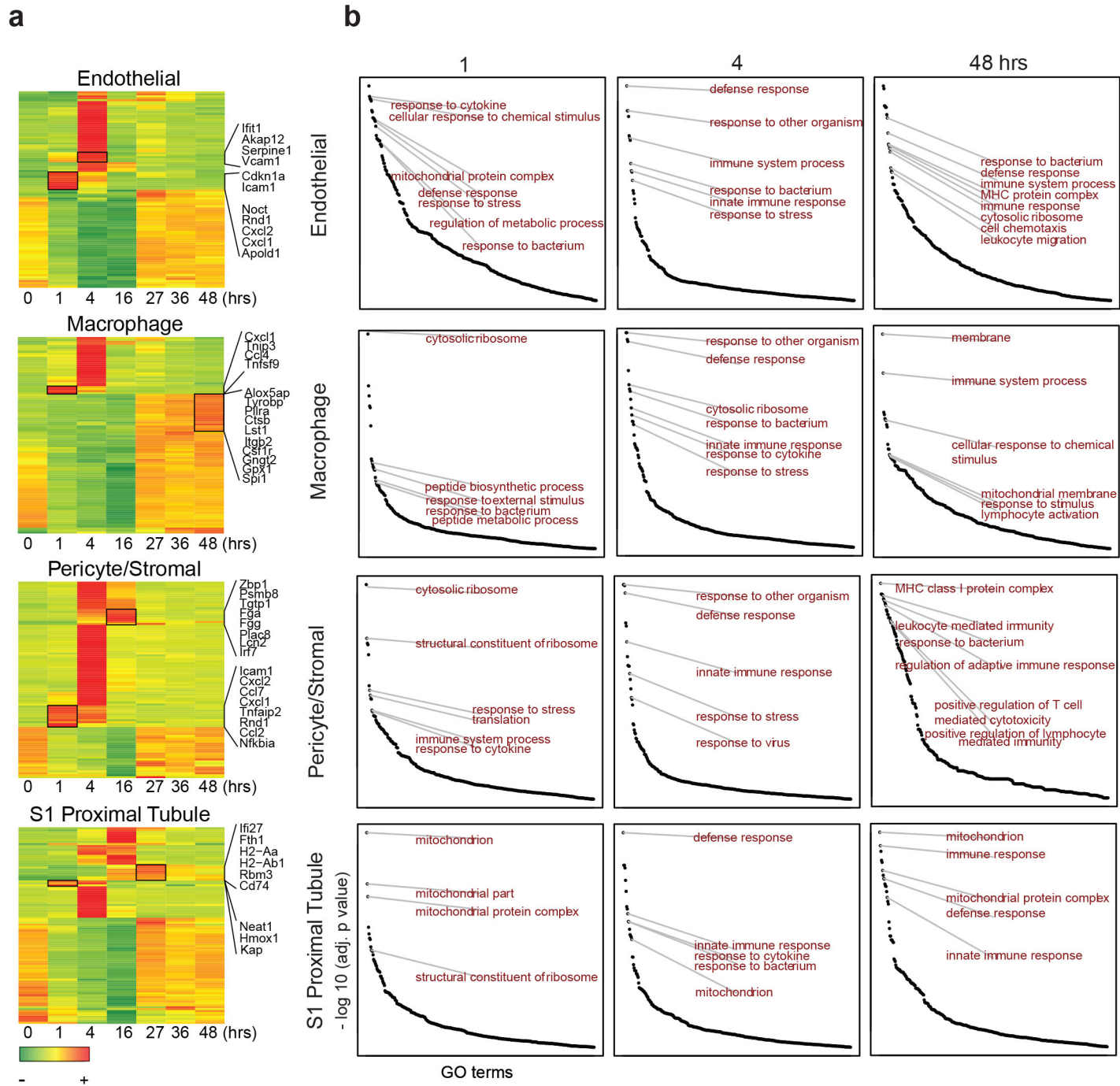


**Fig. 5: Sepsis induces time and cell-specific genes and pathways.** **a** Heatmaps of select cell types with top 100 differentially expressed genes across the sepsis timeline (0-48 hours). Select genes are shown for each cell type. **b** Time dependent enrichment of gene ontology terms for indicated cell types. GO terms are sorted in order of statistical significance. Hrs, hours. GO, gene ontology biological processes

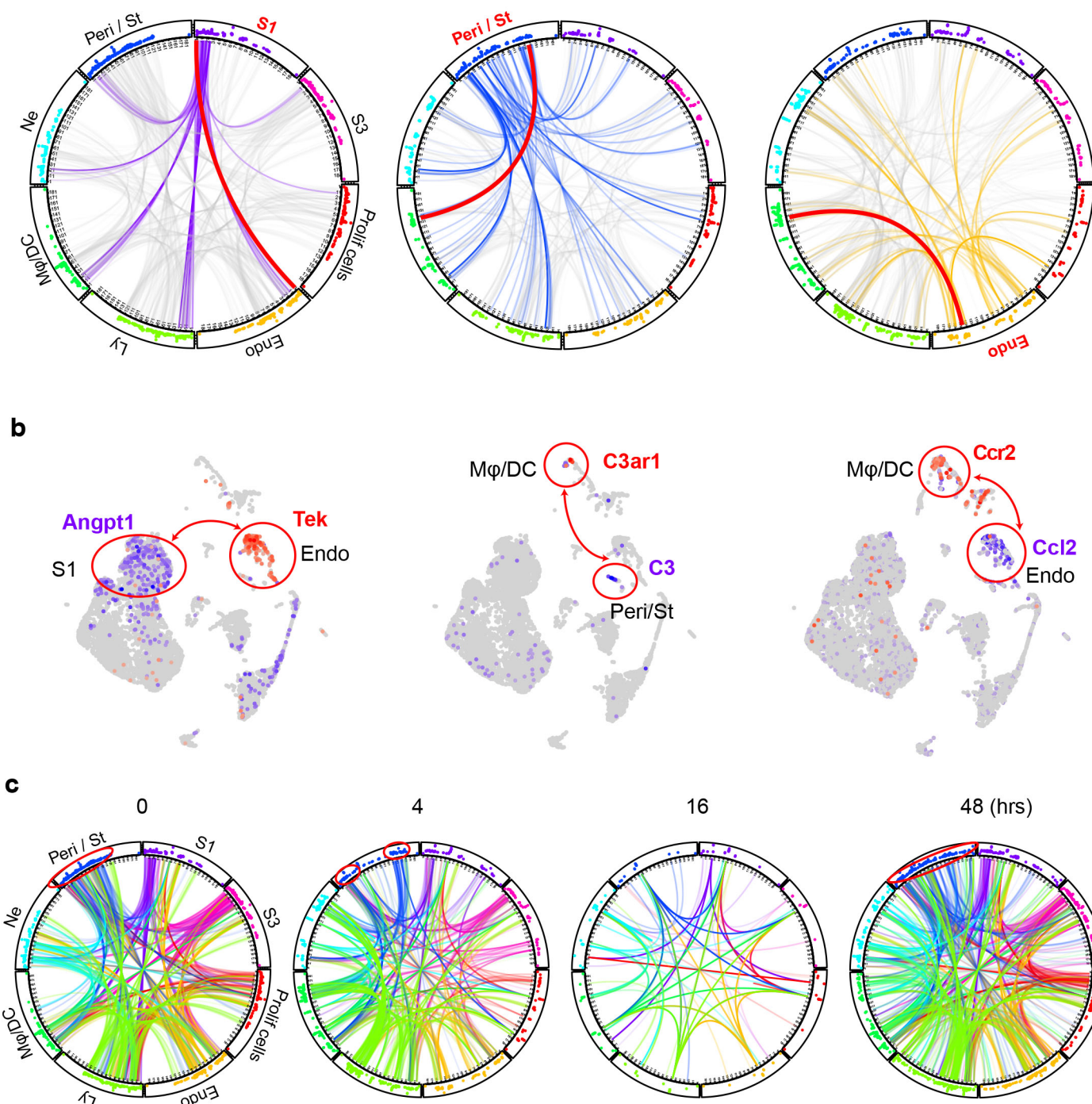


**Fig. 6: Sepsis alters cell-cell communication in the murine kidney.** **a** Receptor-ligand pairs for indicated cell types are displayed in circular plots. The data was generated using the CellPhone database. For clarity, communication between one cell type and all others is shown (purple lines: 0 hr for *S<sub>1</sub>*, blue lines: 1 hr for Peri/St and yellow lines: 4 hrs for endothelial cells). Other cell-cell communications in each circular plot are shown in light grey in the background. In each circular plot, the red line connects the specific receptor-ligand pair highlighted in panel B. Dots in the outer track of the circle represent specific ligands or receptors and are positioned identically for all cell types. The height of dots correlates with statistical significance (all dots are less than adjusted p.value <0.05). The identity of each dot is given in **Supplementary Table 2**.

**b** Feature plots of receptor-ligand pairs between specified cell types as highlighted by the red line in panel A. In each feature plot, the ligand is shown in purple and the receptor in red. **c** Circular plots displaying receptor-ligand interactions between all cell types at specified time points. Examples of change in communication patterns are shown in the red circles in the outer track of the plot at 0, 4 and 48 hours. Note the dramatic drop in cell communication at 16 hours. Endo, endothelial cells. Hrs, hours. Ly, lymphocytes. Mφ-DC, macrophage-dendritic cells. Ne, neutrophil. Peri/St, mixed pericyte and stromal cells. Prolif. Cells, proliferative cells. PT, proximal tubule. *S<sub>1</sub>*, first segment of PT. *S<sub>3</sub>*, third segment of PT.

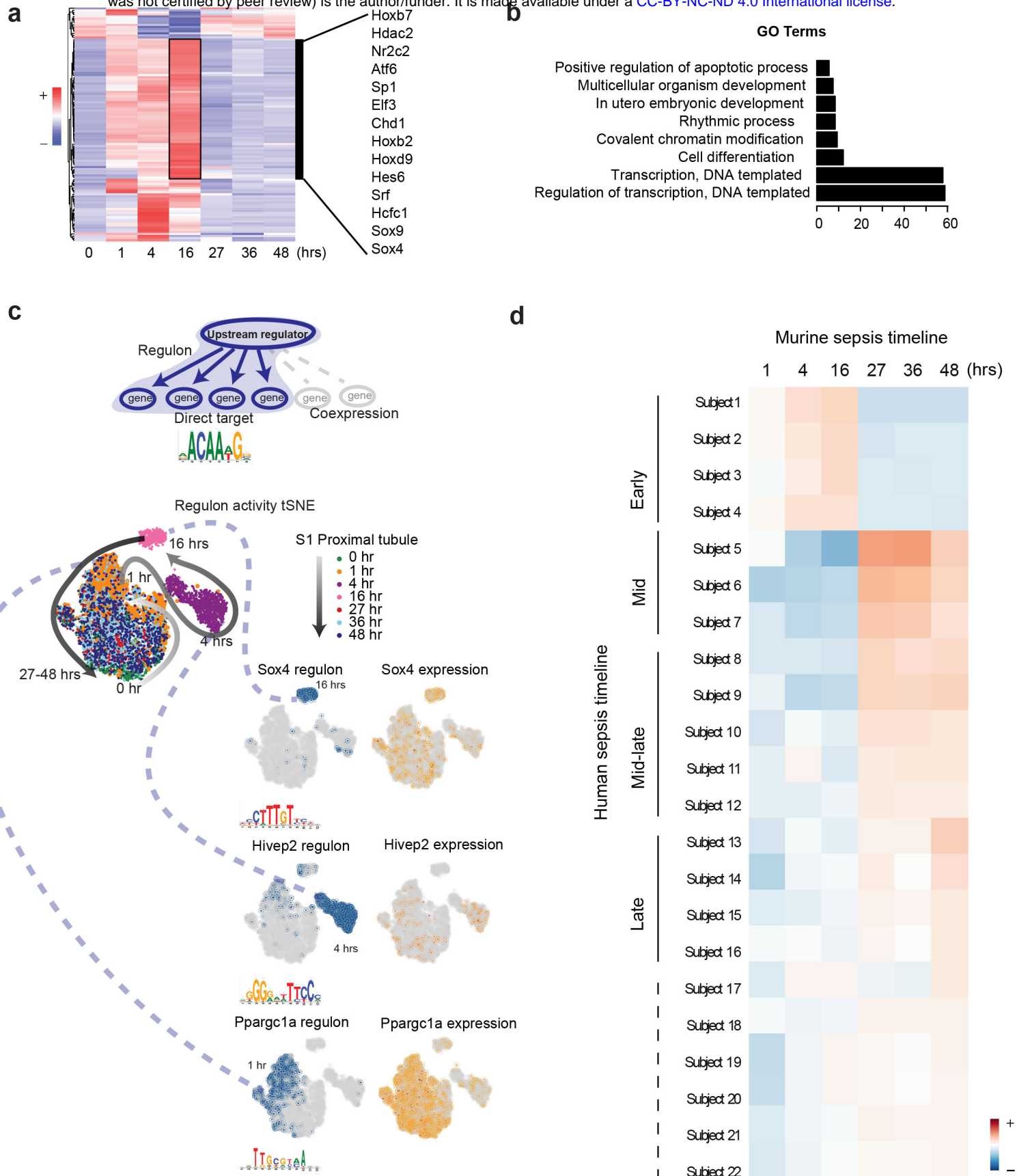
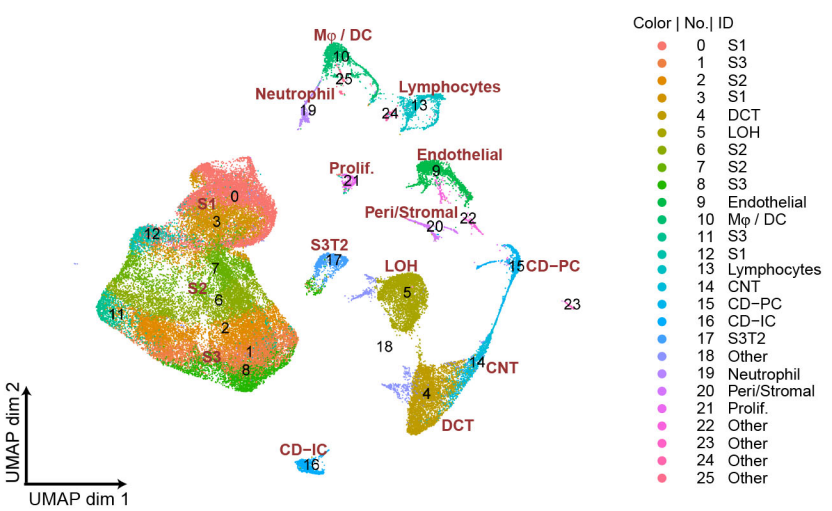
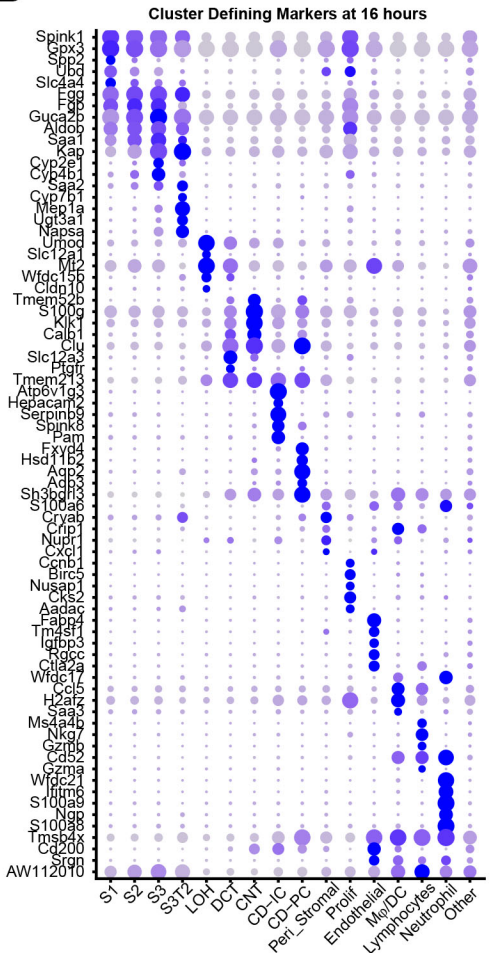


**Fig. 7: Sepsis induces time and cell-specific changes in regulons.** **a** SCENIC-derived heatmap of regulons for S1 tubules. Highlighted are select transcription factors with active regulons at the 16 hour time point. **b** Gene ontology pathway enrichment analysis derived from all regulons active at the 16-hour time point (Tables S4, S5). **c** t-SNE of proximal tubule S1 time-specific regulon activity. Select transcription factor expression (orange) and its corresponding regulon expression (blue) are shown. As shown for Sox4, note the temporal differences between the expression of the transcription factor itself and its regulon. **d** Heatmap of human sepsis kidney samples stratified based on aggregates of murine time-specific orthologues. The color scale indicates the degree of correlation based on Spearman's  $\rho$ . Hr(s), hour(s). GO, gene ontology biological processes.

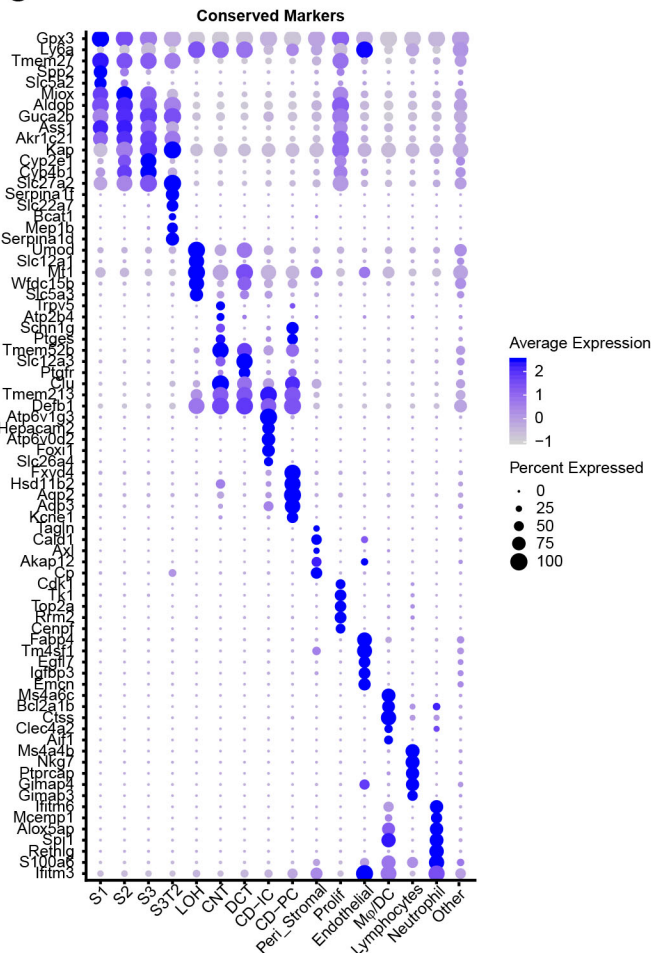
**A**



**B**

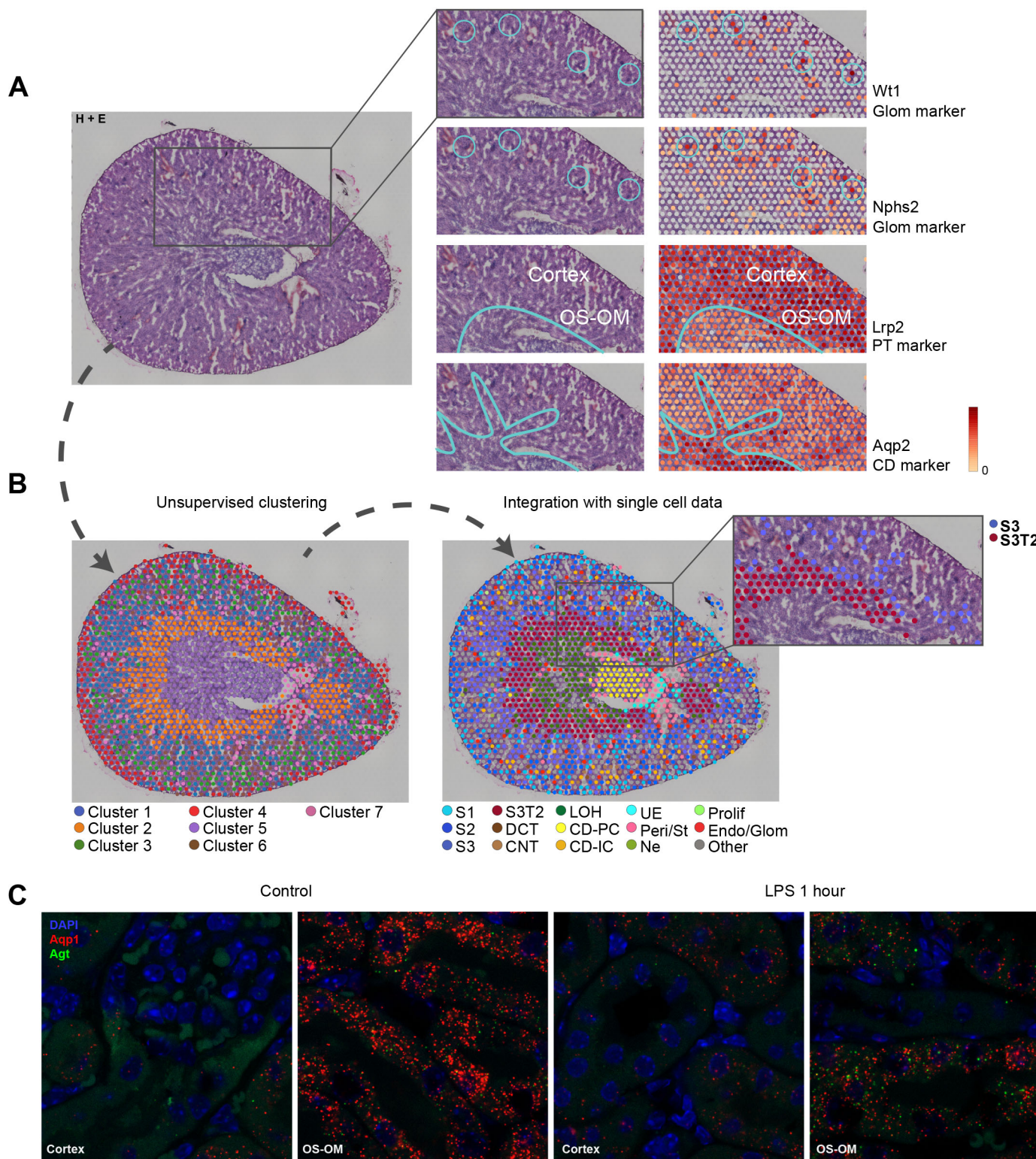


**C**



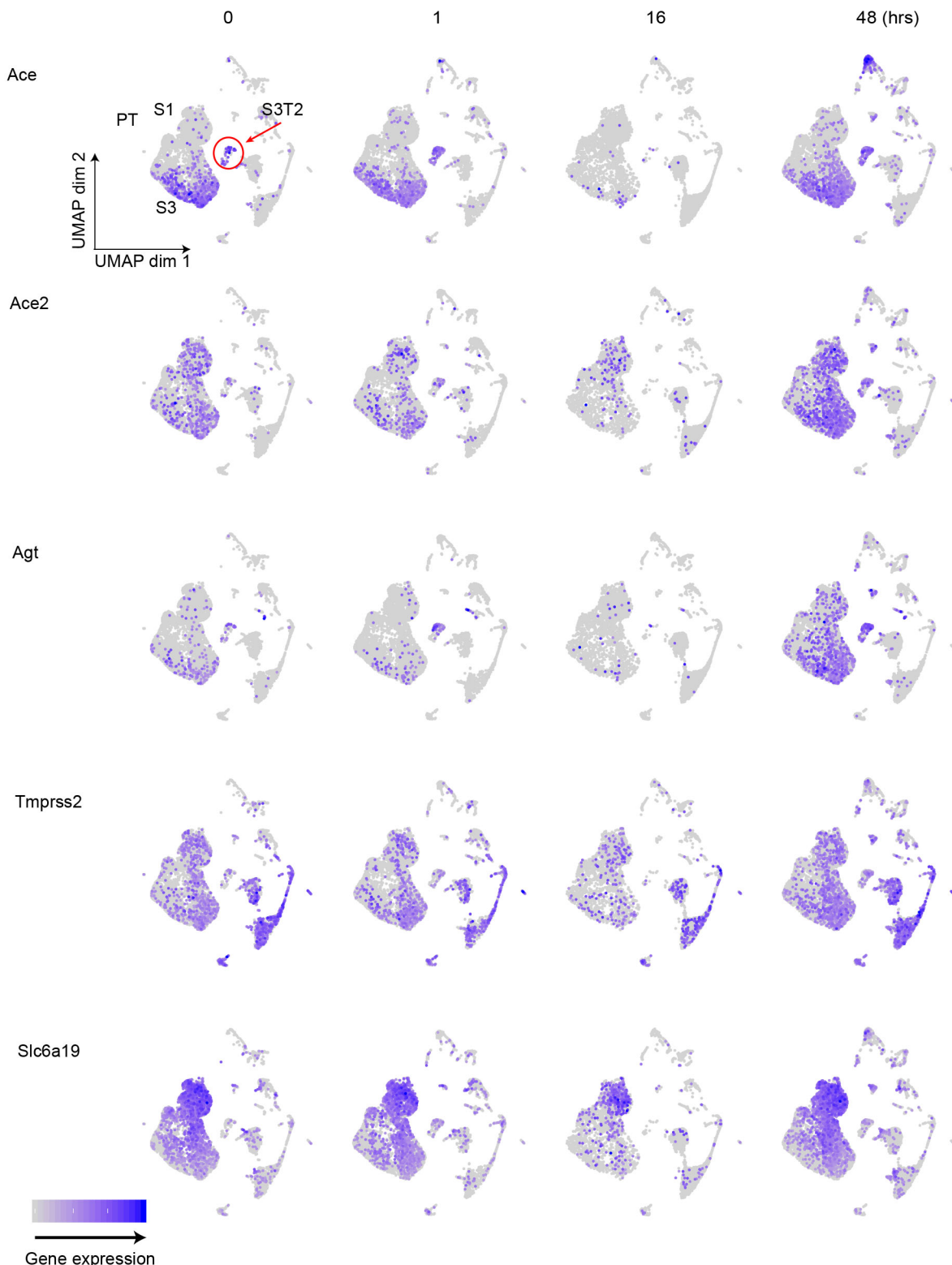
**Supplementary Figure 1. Cluster-defining markers across the sepsis timeline, related to Figure 1.**

(A) Integrated UMAP of kidney cell clusters showing both assigned identity and original cluster number from control and LPS-treated mice (0, 1, 4, 16, 27, 36 and 48 hours after LPS injection). (B-C) Dot plots of top five cluster-defining (shown at 16 hours) and conserved marker genes (all time points integrated). CD, collecting duct. CD-IC, collecting duct-intercalated cells. CD-PC, collecting duct-principle cells. CNT, connecting tubule. DCT, distal convoluted tubule. Endo, endothelial cells. LOH, Loop of Henle. LPS, endotoxin. Ly, lymphocytes. Mp-DC, macrophage-dendritic cells. Ne, neutrophil. Peri/St, mixed pericyte and stromal cells. Prolif. Cells, proliferative cells. PT, proximal tubule. S1, first segment of PT. S2, second segment of PT. S3, third segment of PT. S3T2, S3 type 2 cells.



**Supplementary Figure 2. Spatial transcriptomics validation, related to Figure 2.**

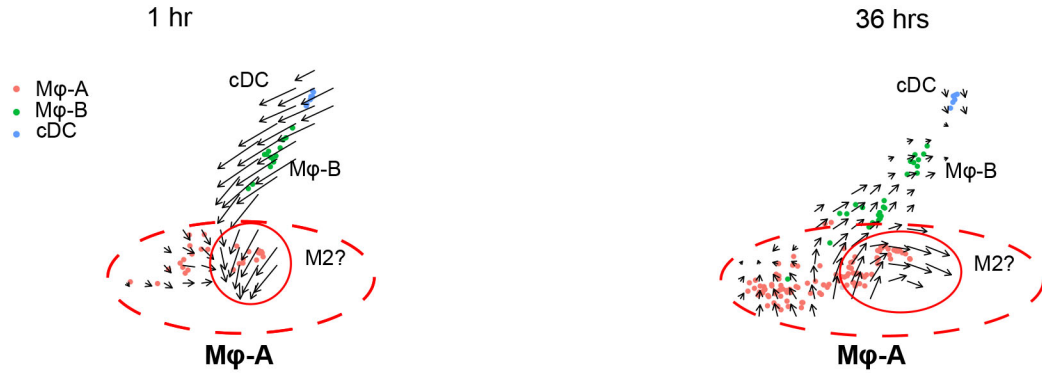
(A-B) Spatial transcriptomics of murine kidney showing unsupervised clustering (B-left) and expanded clustering after integration with single cell data (B-right). Insets of A show gene expression of select glomerular and tubular markers. Inset of B-right highlights S3 and S3T2 clusters. (C) Single molecular FISH (smFISH) coexpression of Aqp1 (red) and Agt (punctate green) in control kidney and after 1 hour of LPS (Cortex and outer stripe of outer medulla shown). Diffuse green objects are RBC and tubular autofluorescence. CD, collecting duct. CD-IC, collecting duct-intercalated cells. CD-PC, collecting duct-principle cells. CNT, connecting tubule. DCT, distal convoluted tubule. Endo/Glom, glomerular endothelial cells. Glom, glomerulus. H+E, hematoxylin and eosin stain. LOH, Loop of Henle. LPS, endotoxin. Ly, lymphocytes. M $\phi$ -DC, macrophage-dendritic cells. Ne, neutrophil. OS-OM, outer stripe of outer medulla. Peri/St, mixed pericyte and stromal cells. Prolif. Cells, proliferative cells. PT, proximal tubule. S1, first segment of PT. S2, second segment of PT. S3, third segment of PT. S3T2, S3 type 2 cells. UE, ureteric epithelium



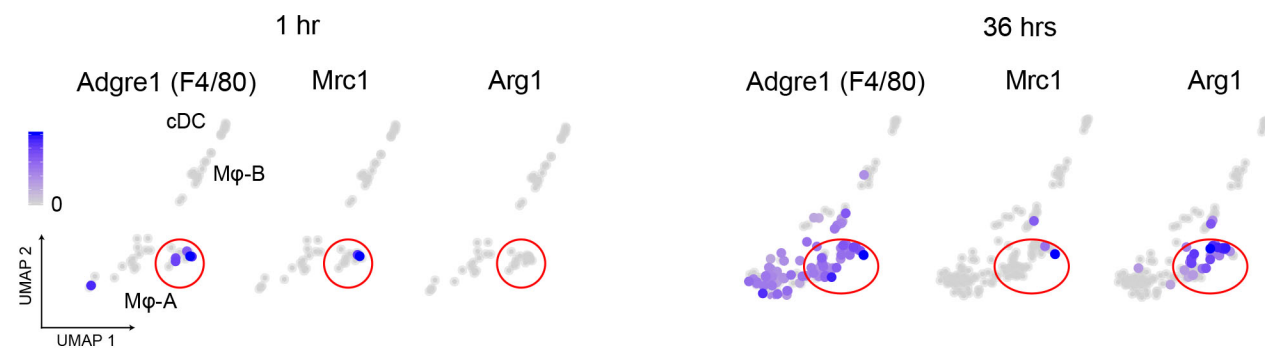
**Supplementary Figure 3. SARS CoV-2 axis, related to Figure 2.**

Feature plots showing expression of SARS CoV-2 related genes at specified time points. Hr(s), hour(s). PT, proximal tubule. S1, first segment of PT. S3, third segment of PT. S3T2, S3 type 2 cells.

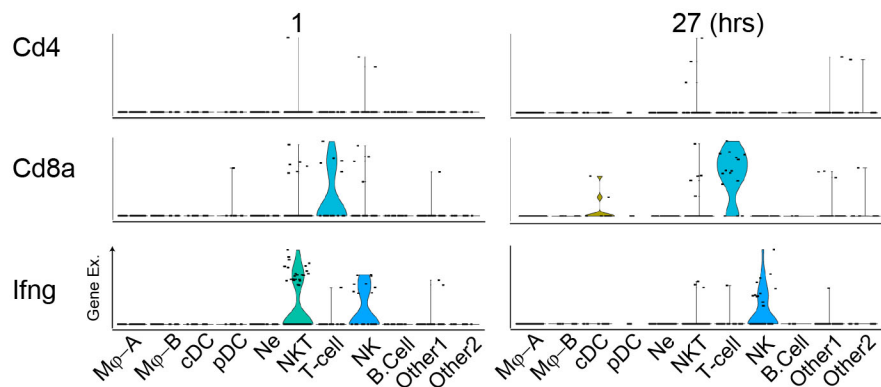
**A**



**B**



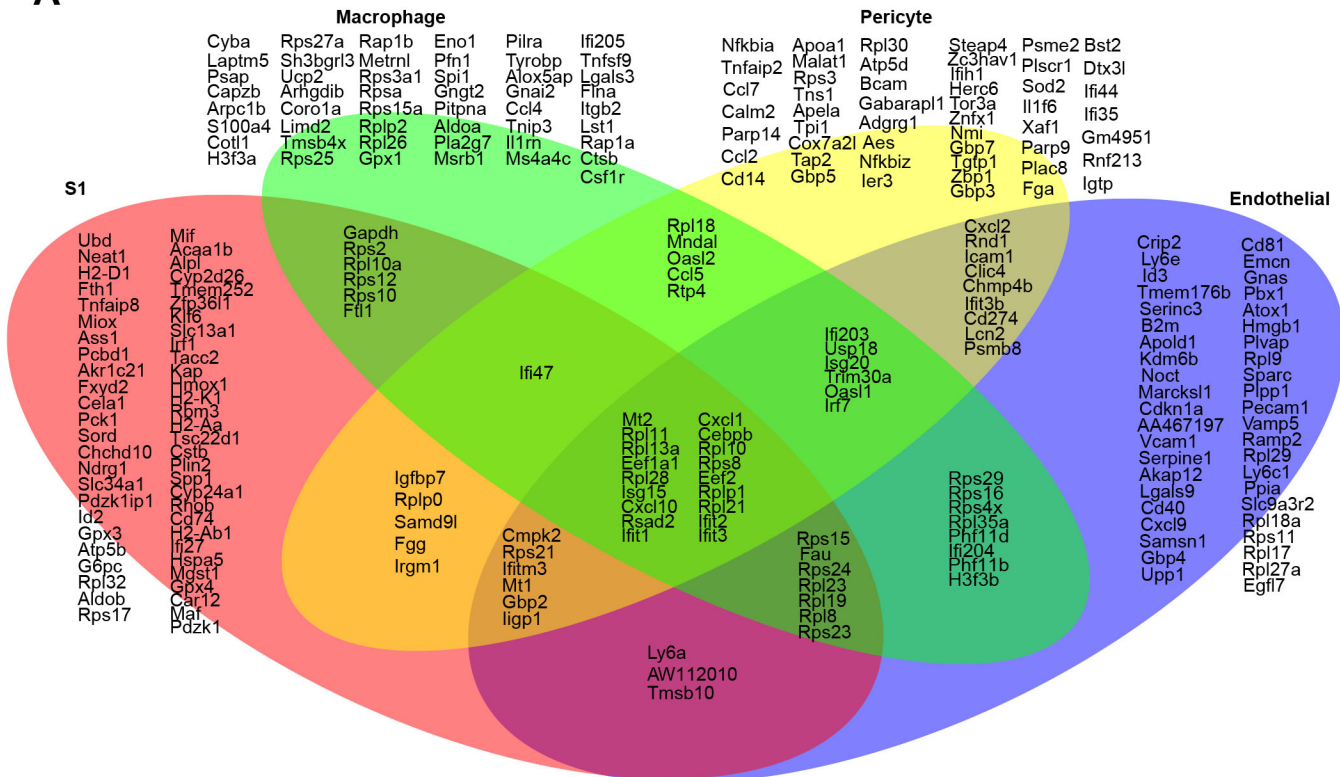
**C**



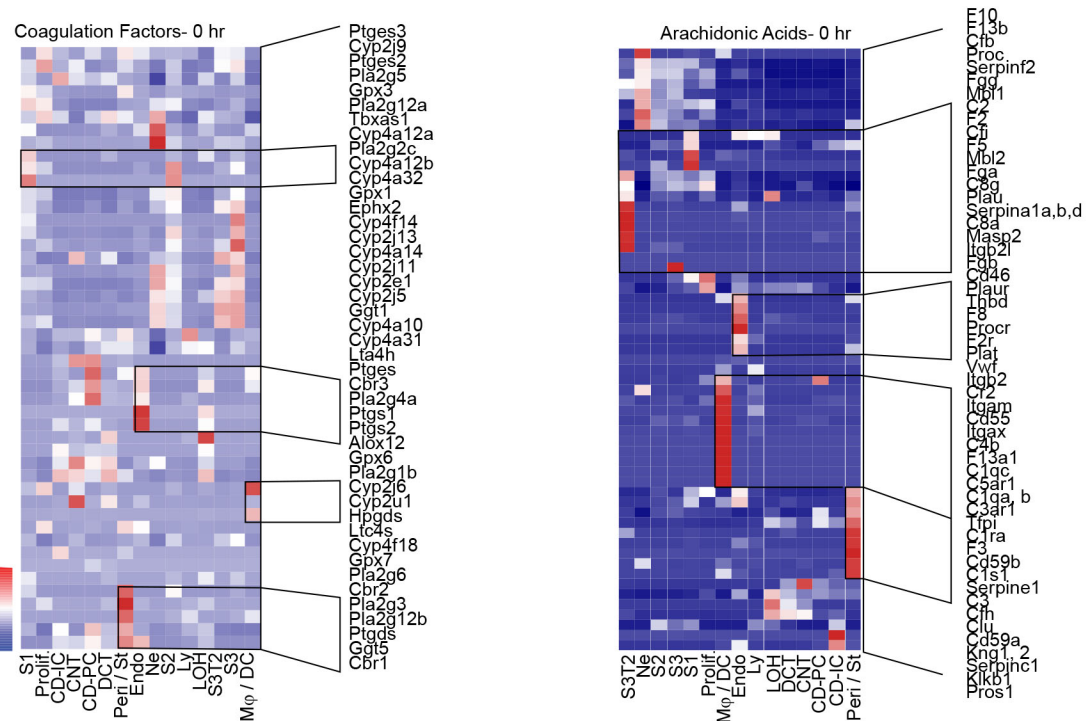
### Supplementary Figure 4. Immune cell subset characteristics, related to Figure 3.

(A) RNA velocity analysis reveals two distinct subfields within the Mφ-A cluster. The subfield circled in red showed expression of M2 macrophage-related genes at later time points (B). (C) Violin plots of Cd4, Cd8 and Ifn-g expression across immune cell subtypes. cDC, conventional dendritic cell. Hrs, hours. Mφ-A, macrophage-A. Mφ-B, macrophage-B. M2, alternatively activated macrophages. Ne, neutrophil. NK, natural killer cells. NKT, natural killer T-cells. pDC, plasmacytoid dendritic cell. T-cell, Cd3+ T-lymphocytes.

**A**

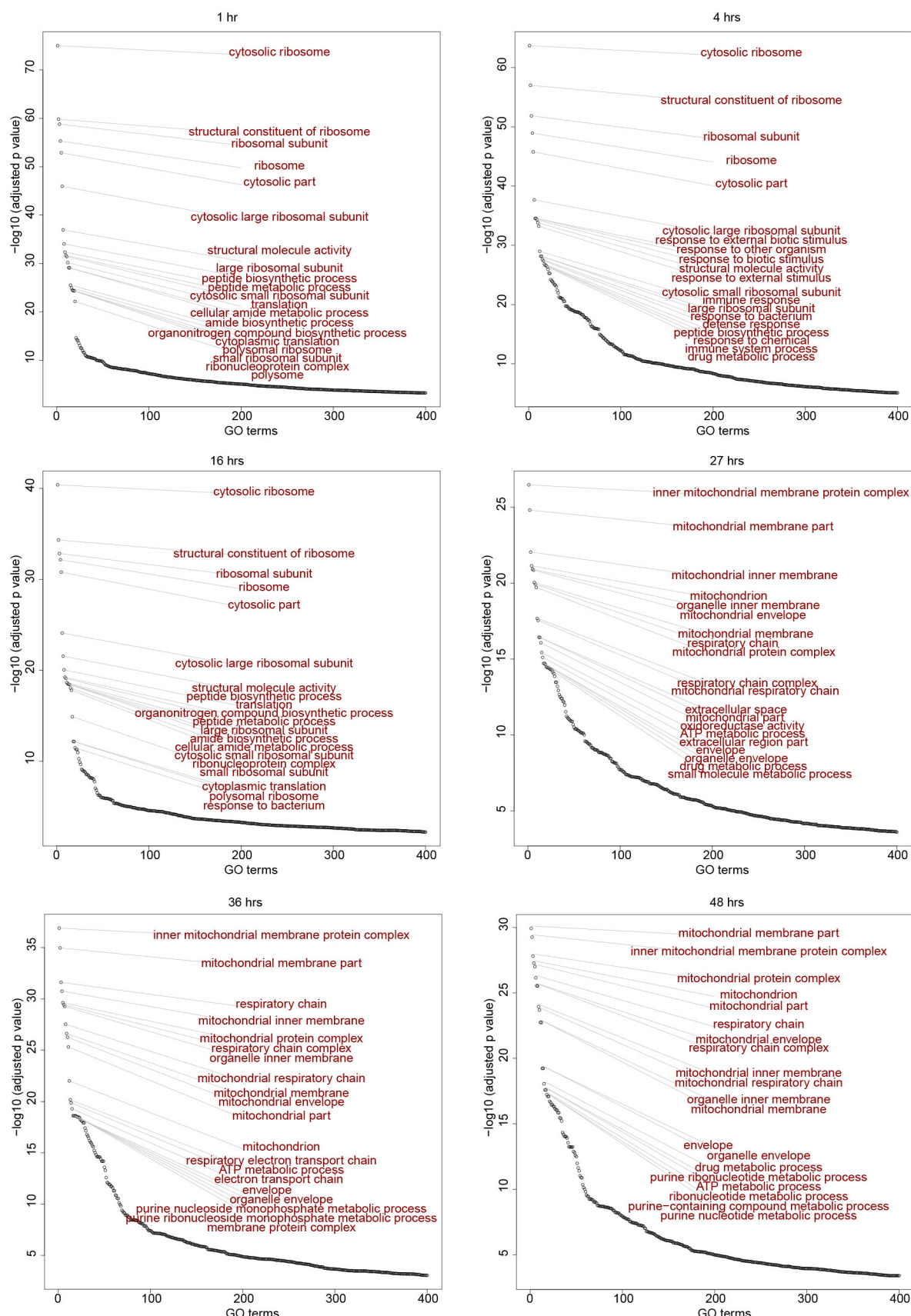


**B**



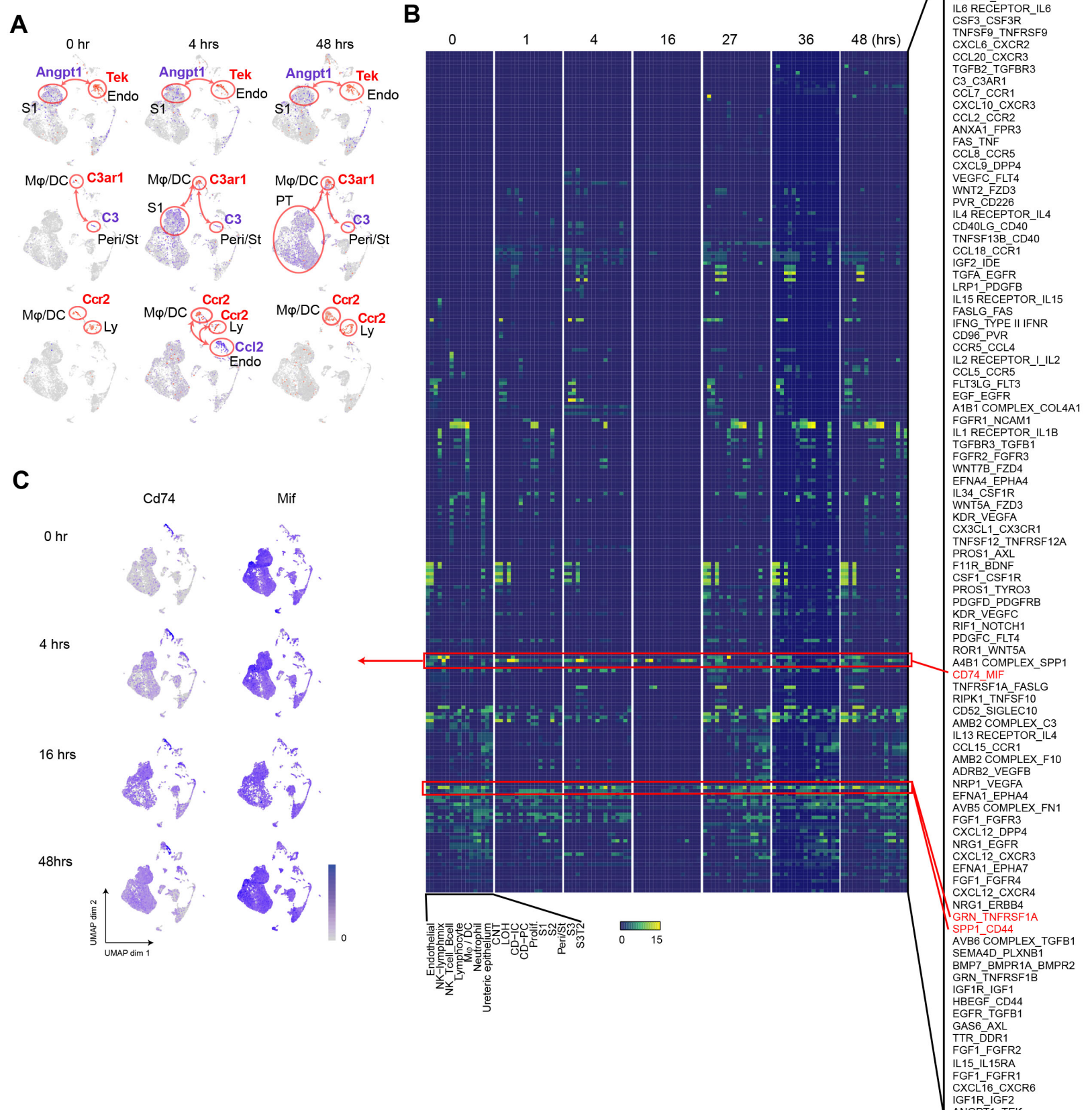
**Supplementary Figure 5. Comparisons of transcriptomic profiles across the sepsis timeline, related to Figure 5.**

(A) Venn diagram showing differentially expressed genes across time (0-48 hours) for indicated cell types. (B) Heatmaps of genes involved in coagulation and arachidonic acid related pathways in all cell types. CD-IC, collecting duct-intercalated cells. CD-PC, collecting duct-principle cells. CNT, connecting tubule. DCT, distal convoluted tubule. Endo, endothelial cells. Hr(s), hour(s). LOH, Loop of Henle. Ly, lymphocytes. M $\phi$ -DC, macrophage-dendritic cells. Ne, neutrophil. Peri/St, mixed pericyte and stromal cells. Prolif., proliferative cells. PT, proximal tubule. S1, first segment of PT. S2, second segment of PT. S3, third segment of PT. S3T2, S3 type 2 cells.



**Supplementary Figure 6. S3 T2 GO terms, related to Figure 5**

Time dependent enrichment of gene ontology terms for S3T2 cells. GO terms are sorted in order of statistical significance. Hr(s), hour(s). GO, gene ontology biological processes. S3T2, S3 type 2 cells.



A9B1\_COMPLEX\_SPP1  
 IL2 RECEPTOR\_HA\_IL2  
 A1B1\_COMPLEX\_COL6A3  
 WNT5A\_FZD2  
 IL6 RECEPTOR\_IL6  
 CSF3\_CSFR3  
 TNFSF9\_TNFRSF9  
 CXCL6\_CXCR2  
 CCL20\_CXCR3  
 TGFB2\_TGFB3  
 C3\_C3AR1  
 CCL7\_CCR1  
 CXCL10\_CXCR3  
 CCL2\_CCR2  
 ANXA1\_FPR3  
 FAS\_TNF  
 CCL8\_CCR5  
 CXCL9\_DPP4  
 VEGFC\_FLT4  
 WNT2\_FZD3  
 PVR\_CD226  
 IL4 RECEPTOR\_IL4  
 CD40LG\_CD40  
 TNFSF13B\_CD40  
 CCL18\_CCR1  
 IGF2\_IDE  
 TGF $\alpha$ \_EGFR  
 LRP1\_PDGFB  
 IL15 RECEPTOR\_IL15  
 FASLG\_FAS  
 IFNG\_TYPE II IFNR  
 CD96\_PVR  
 CCR5\_CCL4  
 IL2 RECEPTOR\_IIL2  
 CCL5\_CCR5  
 FLT3LG\_FLT3  
 EGF\_EGFR  
 A1B1\_COMPLEX\_COL4A1  
 FGFR1\_NCAM1  
 IL1 RECEPTOR\_IL1B  
 TGFBR3\_TGFBR1  
 FGFR2\_FGFR3  
 WNT7B\_FZD4  
 EFNA4\_EPHA4  
 IL34\_CSF1R  
 WNT5A\_FZD3  
 KDR\_VEGFA  
 CX3CL1\_CX3CR1  
 TNFSF12\_TNFRSF12A  
 PROS1\_AXL  
 F11R\_BDNF  
 CSF1\_CSFR1  
 PROS1\_TYRO3  
 PDGFD\_PDGFRB  
 KDR\_VEGFC  
 RIF1\_NOTCH1  
 PDGFC\_FLT4  
 ROR1\_WNT5A  
 A4B1\_COMPLEX\_SPP1  
**Cd74\_Mif**  
 TNFRSF1A\_FASLG  
 RIPK1\_TNFSF10  
 CD52\_SIGLEC10  
 AMB2\_COMPLEX\_C3  
 IL13 RECEPTOR\_IL4  
 CCL15\_CCR1  
 AMB2\_COMPLEX\_F10  
 ADRB2\_VEGFB  
 NRP1\_VEGFA  
 EFNA1\_EPHA4  
 AVB5\_COMPLEX\_FN1  
 FGF1\_FGFR3  
 CXCL12\_DPP4  
 NRG1\_EGFR  
 CXCL12\_CXCR3  
 EFNA1\_EPHA7  
 FGF1\_FGFR4  
 CXCL12\_CXCR4  
 NRG1\_ERBB4  
**GRN\_TNFRSF1A\_SPP1\_CD44**  
 AVB6\_COMPLEX\_TGFB1  
 SEMA4D\_PLXNB1  
 BMP7\_BMPR1A\_BMPR2  
 GRN\_TNFRSF1B  
 IGF1R\_IGF1  
 HBEGF\_CD44  
 EGFR\_TGFB1  
 GAS6\_AXL  
 TTR\_DDR1  
 FGF1\_FGFR2  
 IL15\_IL15RA  
 FGF1\_FGFR1  
 CXCL16\_CXCR6  
 IGF1R\_IGF2  
 ANGPT1\_TEK

**Supplementary Figure 7. Expanded cell-cell communication examples, related to Figure 6.**

(A) Feature plots illustrating cell and time-dependent expression changes of select receptor-ligand pairs. (B) Heatmaps of receptor-ligand pairs at select time points. Red boxes highlight select pairs across time. (C) Feature plots illustrating time dependent expression of Cd74-MIF receptor-ligand pair . CD-IC, collecting duct-intercalated cells. CD-PC, collecting duct-principle cells. CNT, connecting tubule. DCT, distal convoluted tubule. Endo, endothelial cells. Hr(s), hour(s). LOH, Loop of Henle. Ly, lymphocytes. Mφ-DC, macrophage-dendritic cells. Ne, neutrophil. Peri/St, mixed pericyte and stromal cells. Prolif., proliferative cells. PT, proximal tubule. S1, first segment of PT. S2, second segment of PT. S3, third segment of PT. S3T2, S3 type 2 cells.